Modelling Hysteresis in Perovskite / C-Si Tandem Solar Cells

Opto-Electrical Simulations using GenPro4 and Sentaurus

SET3901: Thesis Project

M.J. Chin-On

Delft University of Technology

TU Delft

Modelling Hysteresis in Perovskite / c-Si Tandem Solar Cells

Opto-Electrical Simulations using GenPro4 and Sentaurus

by

M.J. Chin-On

Student Name	Student Number
Maxim Chin-On	4888979

to obtain the degree of Master of Science
at the Delft University of Technology,
to be defended publicly on 27th of August 2024.

Project Duration:	15th of January 2024 - 27th of August 2024
Supervisor:	Dr. ir. Rudi Santbergen
Daily supervisor:	Dr. ir. Paul A. Procel Moya
Internal committee member	Prof. dr. ir. Olindo Isabella
External committee member	Prof. dr. ir. Tom Savenije

An electronic version of this thesis is available at http://repository.tudelft.nl/.

TU Delft

Preface

With this thesis project, my time at TU Delft comes to an end. During my research, my daily-supervisor Dr. ir. Paul Procel Moya was of enormous help and I would like to thank him for our discussions and his guidance. I want to thank Dr. ir. Rudi Santbergen for making it possible for me to research this topic and be a temporary member of the PVMD group. Furthermore, thank you to the other committee members for being part of my examination committee, Prof. dr. ir. Olindo Isabella and Prof. dr. ir. Tom Savenije.

M.J. Chin-On
Delft, August 2024

Abstract

As the energy demand keeps rising and the need for clean, affordable energy increases, the switch to completely sustainable energy production comes closer and closer. Solar cells are expected to play a big role in this energy transition. However, the technology of the most used type of solar cell, crystalline silicon, is nearing its limit. This calls for other novel technologies that could surpass it. One of these promising technologies is the perovskite / c-Si tandem cell.

This type of cell has shown promising results in recent years, but for it to be commercialized and challenge the current technologies that dominate the market, some steps need to be taken. This thesis focuses on hysteresis, a behaviour commonly shown in perovskite cells, resulting in an uncertainty when measuring the characteristics of these cells.

The most common explanation for this behaviour has been due to ion migration under certain conditions. This report, however, looks at hysteresis from a different perspective. It investigates the effect of defects on the hysteresis behaviour, continuing on previous research on this mechanism. It is argued that the defects trap charge near the interfaces, affecting the charge extraction and with that the amount of recombination in the cell. This hypothesis is researched by modelling a state-of-the-art perovskite / c-Si tandem cell in TCAD Sentaurus.

This research investigates multiple important parameters to these defects, such as defect density, distribution, energy level, and capture cross-section. With these variables, the hysteresis behaviour as a result of the defects is explored. These results are then used to compare the hysteresis behaviour of the tandem cell with a similar single-junction cell, after which the difference between the two is analysed.

It is found the two types of cells have similar hysteresis behaviours, but not equal. With the main deviation finding its origin in the current-limiting that can be displayed by tandem cells.

Contents

List of Figures

List of Tables

Acronyms

Abbreviation	Definition
c-Si	Crystalline silicon
PV	Photovoltaic
PCE	Power conversion efficiency
TCO	Transparent conductive layer
HTL	Hole transport layer
ETL	Electron transport layer
HSC	Hole selective contact
ESC	Electron selective contact
ARC	Anti reflective coating
TRJ	Tunnel recombination junction
CSC	Carrier selective contact
TCAD	Technology computer aided design
SDE	Sentaurus structure editor
SDEVICE	Sentaurus device
SVISUAL	Sentaurus visual
SRH	Shockley-Read-Hall
2T	Two terminal
EQE	External quantum efficiency
SJ	Single-junction
sr	Scan rate
HI	Hysteresis index

1 Introduction

Ever since the dawn of human existence, the sun has provided mankind with warmth. It has made it possible for life to thrive and develop into what our planet is now. With the discovery of the photovoltaic effect, the sun does not only provide us with warmth anymore, but now its energy can be converted into electricity as well. As we face challenges to make the switch to sustainable energy sources, this discovery has paved the path towards devices that can convert the energy from photons emitted by the sun to electricity: solar cells.

This thesis will delve deeper into the workings of a specific type of novel solar cell. By combining two absorber layers, made up of perovskite and crystalline silicon (c-Si), a tandem cell is made. This tandem cell will be simulated and researched to better understand how it behaves to ultimately improve the cells performance.

This chapter will first delve deeper into the background of photovoltaic (PV) technology in Section 1.1. The next section (1.2) will explain the reasoning for perovskite / c-Si tandem cells, explain a standard cell, and set out the technology's challenges. Section 1.3 will shortly introduce an important unwanted physical behaviour in perovskite cells. The simulation softwares used are to be presented in Section 1.4. Lastly the project description and outline will be discussed in Section 1.5.

1.1. Background

The stepping stone for modern photovoltaic technology is the discovery of the photovoltaic effect by Becquerel in 1839 [1]. The photovoltaic is described as the generation of a voltage and an electric current in a material when illuminated with light. Although, from its discovery, it would still take many years for the effect to be fully explained by Albert Einstein [2]. He stated that a certain unit of light, later called a photon, carried an amount of energy based on its frequency. Even though the first demonstration of the photovoltaic effect in a junction was shown by William Grylls Adams in 1876, the first practical solar cell was developed by Bell Laboratories in 1954 with an efficiency of 6% [1]. From that point more and more research was dedicated towards the solar cell, and the need for more renewable energy sources in the last decades has catalysed the rapid growth of this sector.

The main focus in this sector has been on the crystalline silicon (c-Si) solar panel, making up 95% of the installed capacity in 2021 [3]. Silicon makes up more than a quarter of the earth's crust [4], making it a relatively cheap product to fabricate solar cells from. On top of that, it has been proven sufficiently durable over the years with most lifetimes of 25 years and over. It is an established technology with years of research backing it up.

But now this technology is approaching its maximum power conversion efficiency (PCE), set by the Shockley-Queisser limit [5]. This calls for new technologies that can surpass c-Si cells. As for this, many look towards multi-junction solar cells since they have shown a lot of improvements and potential as shown in Figure 1.1. These cells use the different bandgaps of materials to more efficiently capture the

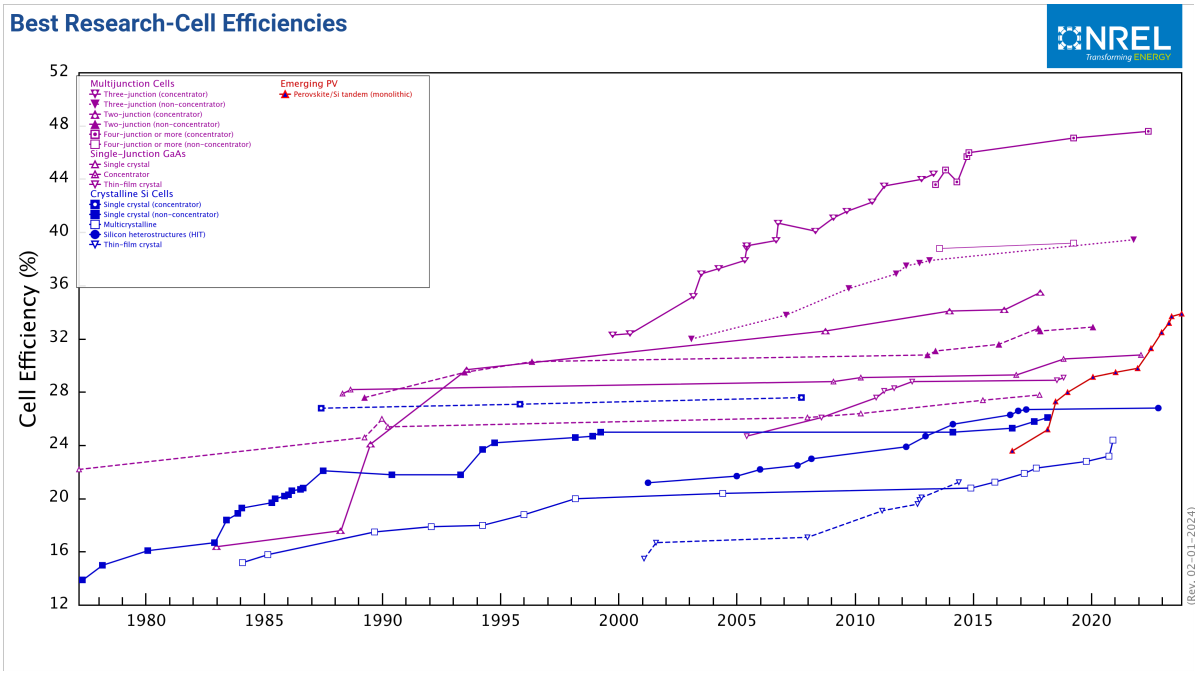

Figure 1.1: A graph showing the best research-cell efficiencies throughout the years with c-Si cells in blue, general multi-junction cells in purple and perovskite/c-Si tandems in red [6]

solar spectrum. One of these promising multi-junction technologies is the perovskite / c-Si tandem cell. In the figure, the purple data-points represent general multi-junction cells, blue c-Si cells, and red perovskite /c-Si tandem cells.

When two absorber materials are stacked vertically, they are in tandem configuration. This makes it possible to achieve higher PCE's than a single-junction device would reach as well as reducing degradation effects [7]. When configured correctly, the top cell absorbs a certain part of the light spectrum, and lets photons with a higher wavelength through to be absorbed by the second cell. This is the ideal case, but in reality there are a lot of variables that need to be optimized to get a working cell. First of all, the two absorber materials need to compliment each other to ensure efficient behaviour. Crystalline silicon is a good choice for the bottom cell because of electrical properties and since it is a very mature technology. One of the possible candidates for the top cell is perovskite.

1.2. Perovskite / c-Si tandem cells

Perovskite is named after L.A. Perovski, a Russian mineralogist [8]. Perovskites are materials that follow the structure of calcium titanate. They all fall under the ABX_3 formula. In this formula, both A & B resemble cations, with A being larger than B, and X is an anion. A cation is an ion with more protons than electrons, and an anion is an ion with more electrons than protons. The structure of perovskite materials can be seen in Figure 1.2.

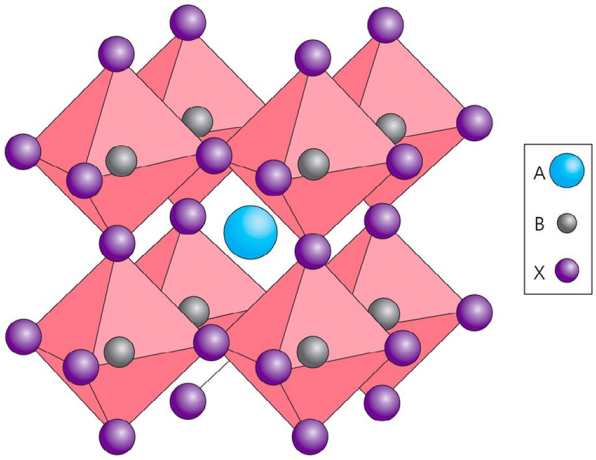

Figure 1.2: The general structure of perovskite materials [9]

The major reason for the use of perovskite as an absorber material is its unique combination of properties making it a stellar candidate. It has a high absorption coefficient, low exciton binding energy, bipolar charge transport and long carrier diffusion length [10, 11, 12, 13]. On top of that its bandgap can be tuned to ensure efficient power conversion [14]. Because of these properties, many researches were conducted on both single-junction perovskite as tandem perovskite solar cells in the last few years.

To highlight the speed of developments in the last years, a list of record breaking solar cells can be seen in Table 1.1. It can be seen that in just a few years time the record PCE of this technology has increased with over 40%. As research has shown that PCE's of above 41% are possible [15], this technology shows a lot of potential growth for the coming years.

Table 1.1: Record breaking perovskite / c-Si monolithic tandem solar cell PCE's of the recent years [6]

Year	Manufacturer	PCE [%]
2016	Stanford / ASU	23.6%
2018	EPFL	25.2%
	Oxford PV	27.3%
2019	Oxford PV	28.0%
2020	HZB	29.15%
2021	Oxford PV	29.5%
	HZB	29.8%
2022	EPFL / CSEM	31.3%
	HZB	32.5%
2023	KAUST	33.2%
	KAUST	33.6%
	LONGi	33.9%
2024	LONGi	34.6%

1.2.1. Cell architecture

To better understand this type of solar cell, a schematic for a general perovskite / c-Si tandem cell is shown in this section. This can be seen in Figure 1.3. The general schematic consists of, from top to bottom as seen in the figure, the electrodes, transparent conductive layer (TCO), hole transport layer (HTL), perovskite absorber layer , electron transport layer (ETL), an interconnection layer, hole selective contact (HSC), c-Si absorber layer, electron selective contact (ESC), and the rear electrode. Other layers can be added such as an anti reflective coating (ARC) or passivisation layers.

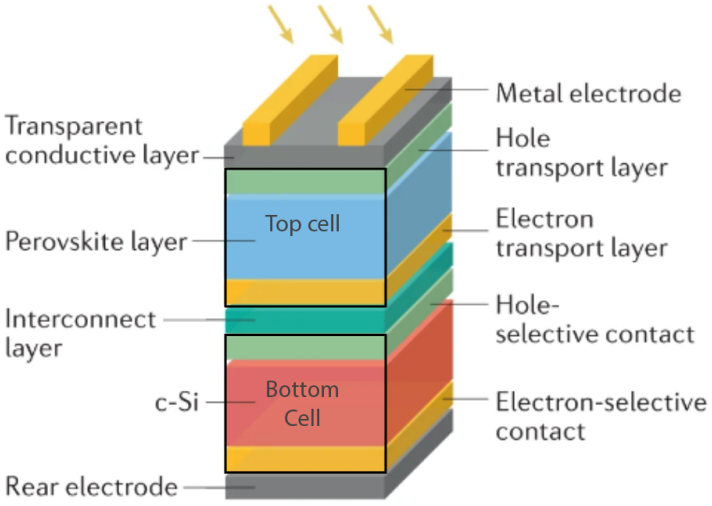

Figure 1.3: A schematic for a general perovskite / c-Si tandem cell in n-i-p configuration [16]

The front and back electrodes are responsible for transporting the generated current out of the cells to be used or stored. It should have a good conductivity to omit resistive losses. Silver (Ag) can be found as the electrode material in most c-Si solar panels [17]. It has also been used in perovskite / c-Si tandem solar cells, but has been shown to react with iodine resulting in irreversible degradation of the cell performance [18]. Other materials viable for electrodes include, but are not limited to, copper (Cu) or TCO materials [19]. TCO materials have the advantage that they are transparent for most wavelengths, increasing the effective area of the solar cell.

The TCO is responsible for conducting the charge carriers from the HTL (or ETL if the cell is inverted) to the electrodes. Since the transport layers usually are not great at lateral movement, the TCO is needed [1]. The second important feature of this layer is that it must be transparent for most of the solar spectrum to avoid parasitic losses. Some materials that are generally used for TCO's in perovskite / c-Si cells are annealed indium oxides doped with Sn, Zn or Zr (ITO, IZO and IZrO respectively) [20].

The HTL's main task is to collect the holes from the absorber layer and transport them to the TCO or electrodes whilst repelling electrons. The HTL should possess four main properties. The HTL should have a large conductance band offset and a small valence band offset to ensure good transportation of holes while blocking electrons. Furthermore it should have a high hole mobility and photo-chemical stability. It should have good solubility in organic solvents and film-forming ability to fit the fabrication process of PSCs. On top of that the HTL should also protect the perovskite from degrading due to humidity and other factors. Lastly it should have a low absorption coefficient to emit parasitic losses [21, 22, 23, 24]. The materials used for HTLs can be divided in two groups, organic and inorganic. Inorganic materials that are regularly used are CuI [25], Cu_20 [26], NiO [27], CuSCN [28]. Whereas organic HTLs consist of small molecular compounds [29], like 2,2',7,7'-tetrakis(N,N-di-p-methoxyphenylamine)-9,9'-spirobifluorene (spiro-OMeTAD), and conducting polymers [30], such as poly(3-hexylthiophene-2,5-diyl) (P3HT).

As stated before, metal halide perovskites show great characteristics for these type of solar cells. They have good absorption coefficients, long diffusion lengths and a tunable bandgap as explained at the beginning of Section 1.2. The perovskite layer in this technology usually consists of methylammonium lead iodide perovskite ($MAPBI_3$) [31]. Recent studies have shown triple cation perovskite (3Cat), $Cs_{0.05}(FA_{0.77}MA_{0.23})_{0.95}Pb(I_{0.77}Br_{0.23})_3$, and triple-halide perovskite (3Hal), $Cs_{0.22}FA_{0.78}Pb(I_{0.85}Br_{0.15})_3$ + 5% $MAPbCl_3$, to be good candidates as well [32, 33]. The latter, 3Hal, is said to improve stability [34] and minimize phase segregation [35] by increasing the the quality of the perovskite lattice.

The ETL has similar requirements as the HTL. The energy band properties are inverse from the HTL, so there should be a large valence band offset and a small conductance band offset to ensure that electrons are let through and holes are repelled. It should have a good electron mobility and be suitable for

deposition on these films. It would be beneficial if the ETL would also protect the absorber layer from degradation. And just as the HTL, low absorption coefficients are key to avoid parasitic losses [36]. The material for ETLs usually consist of a metal oxide such as TiO_2, ZnO, WO_3, ZrO_2, SnO_2, ZnO_2 [37].

The interconnect layer, or tunnel recombination junction (TRJ), connects the top and bottom cell in series. Here, the charge carriers collected from the bottom of the perovskite cell, recombine with the charge carriers collected from the front of the silicon cell [38]. Majority-carrier recombination in this junction is made possible by using quantum-mechanical tunneling of electrons through classically forbidden regions [39]. Recombination in this layer can be divided into good and bad recombination. Since the layer is meant to allow majority charge carriers from the top and bottom cell to recombine, this is classified as good recombination. Bad recombination on the other hand symbolizes recombination from charge carriers originating from the same cell. Materials with a low mobility gap favor good recombination [38]. On top of that, the absorption coefficient of materials needs to be considered to minimize parasitic absorption losses just as in the other layers.

The carrier selective contacts (CSC) in the bottom cell, hole-selective contact (HSC) and electron-selective contact (ESC), follow the main properties of the HTL and ETL of the top cell. They need a good carrier selectivity for their respective majority charge carriers and need to mitigate parasitic absorption [40]. The CSC could be made up out of heavily doped silicon [41], or various other materials such as metal oxides [42], nitrides [43], fluorides [44] and organic materials [45]. These alternatives have been shown to be good candidates based on costs, absorption coefficients and carrier selectivity.

1.2.2. Challenges

The biggest challenge for any novel technology is commercialisation, if it is not an improvement on the in-use technologies, it is not likely to be successful. Even though this technology has shown a lot of improvement and potential, there are still challenges that need to be taken care of before it can be commercialised. First of all, the rapid increase of the device PCE becomes insignificant with the stability issues this technology has been facing. Perovskite-type hybrids are very sensitive to moisture [14] and have shown poor thermal stability [46]. Although research has been done to increase the lifetime of perovskite / c-Si tandem cells, it still is nowhere near the lifetime of commercialised c-Si panels [18]. On top of that, the perovskite /c-Si tandem cells also suffer from light induced instability and phase segregation [47, 48]

A second issue is the use of lead (Pb) as one of the main components in these types of solar cells. Lead leakage could lead to risks for both ecosystem and humans because of its toxicity [49]. Alternatives for lead have been researched but so far have been unable to replicate the high PCE values and relative stability [50]. So it seems lead is necessary to produce commercializable devices, but the health of both human and nature should be taken into account.

Lastly, when measuring perovskite / c-Si tandem cells, the J-V curves sometimes seem to differ when comparing measurements in either forward or reverse scan [51]. A J-V curve is normally a very good way to estimate solar cell performance. In this case, however, it comes with uncertainty since these two methods for measuring come up with different outputs. This means it is unclear what the device PCE and the actual characteristics of the device are. This problem is called hysteresis.

1.3. Hysteresis

The deviating results of the J-V graphs under forward and reverse scan can lead to both over- and underestimating of the characteristics of the solar cell, this phenomenon is known as hysteresis. The effect of hysteresis on a general J-V graph can be seen in Figure 1.4. It can be noted that the V_{mpp}, the voltage for which the power output is the highest, of the reverse scan is higher than that of the forward scan, making the efficiency uncertain. In this example, the reverse scan looks similar to the hysteresis-free J-V graph, this is not necessarily the case for all instances of hysteresis. Hysteresis in perovskite materials can be divided into three categories, normal hysteresis, hysteresis-free, and inverted hysteresis. Inverted hysteresis describes the case where the forward scan shows better characteristics as opposed to the reverse scan [52].

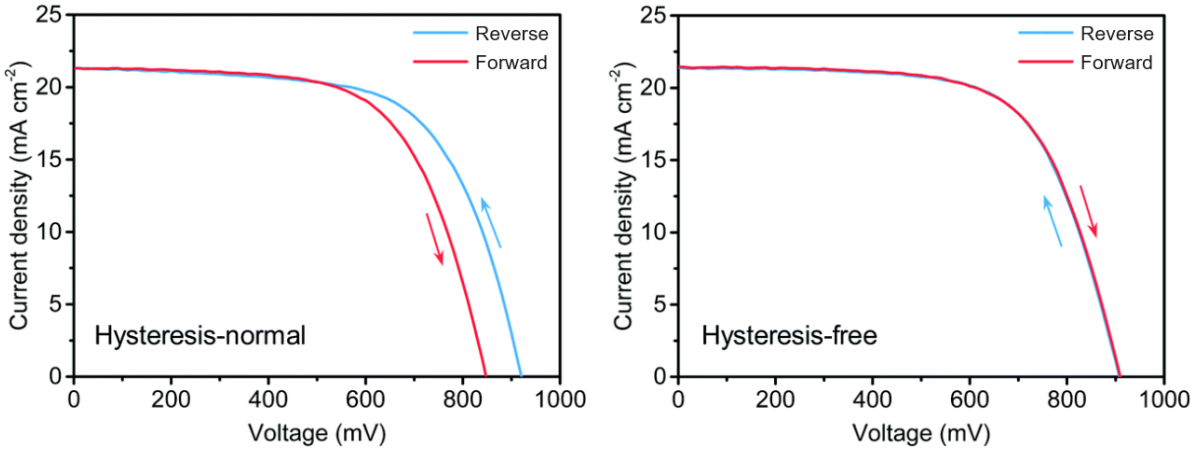

Figure 1.4: Two J-V graphs depicting normal hysteresis (left) and hysteresis-free (right) behaviour [53]

The amount of hysteresis shown in cells affected by has so far been linked to the scan rate, bias voltage preconditioning, device structure, scan direction, and light soaking [54]. However, the full explanation of the behaviour has eluded researchers so far. The most common explanation is ion migration [55, 56, 57, 58, 59]. However, ion migration can not be used to explain hysteresis fully. Other possible explanations include defects at the perovskite interfaces [60, 61, 62, 63, 64], capacitive effects [65, 66, 67], and ferroelectric polarization [68, 69, 70].

This report will research the effect of defects on hysteresis. It builds on the findings of Heerden et al. [63], where hysteresis was modelled using defects in a single-junction perovskite cell. Since the results of this work seemed promising, the same approach will be used to research hysteresis in a tandem cell in this report. Although a few papers have used the defect approach to model hysteresis in single-junction cells, there is a lack of research into modelling hysteresis with trap states in tandem cells.

Completely understanding and possibly solving the hysteresis in perovskite semiconductors would make comparing them straightforward and could help with improving stability. Wu et al. and Cui et al. have shown that decreased hysteresis goes hand-in-hand with an improved stability [71, 72].

1.4. Simulation software

Simulating PV cells has many advantages over fabricating and measuring a physical version. Physically making each iteration of a solar cell is time and resource consuming, and on top of that, it is hard to tell what is going on inside the physical cell when measuring. Using simulations, small changes can be made and the inner workings can be researched more straightforward. During this project, the simulations will be done in TCAD Sentaurus. Technology computer aided design (TCAD) has been widely used in this sector and has proven its effectiveness [73, 74, 63, 75, 76]

To correctly model the generation profile of the device, an optical simulator has to be used. This is implemented by integrating GenPro4 in Sentaurus using the MATLAB tool. GenPro4 is an optical model for solar cells developed by the PVMD group of TU Delft [77]. It combines wave and ray-optics to calculate the fraction of light absorbed, transmitted and reflected by each layer.

TCAD Sentaurus is a tool used for designing and simulating semiconductor devices. This simulation software offers multiple tools for creating these simulations. The tools mostly used in this project are Sentaurus Structure Editor (SDE), Sentaurus Device (SDEVICE), and Sentaurus Visual (SVISUAL). SDE is used to set up the cell structure and materials. To correctly set the material parameters, an additional tool is used, MatPar. SDEVICE simulates the electrical characteristics of the cell using an array of equations. The results from SDEVICE are then processed by SVISUAL to be able to visualize the computed data. Lastly, MATLAB is integrated into the program to process data into solar cell characteristics such as efficiency and fill factor.

1.5. Project objectives and outline

The main goal of this report is to deepen the understanding of hysteresis, specifically in tandem cells. This will be done by creating a realistic model of a perovskite / c-Si tandem cell. This model will then be used to research certain behaviours in these type of cells and compare it to hysteresis in single-junction devices. For this research, the main interest lies in the perovskite layer. By the end of the project, these questions have to be answered:

i Can we simulate hysteresis behaviour in a perovskite / c-Si tandem cell using defects?
ii Does the tandem cell behaviour differ from the single-junction cell, and why?
iii Can we explain the hysteresis behaviour as a result of defects?

Chapter 2 will explain the essential semiconductor physics of solar cells to better understand the important behaviours in the perovskite / c-Si tandem cell. In Chapter 3 the methodology of simulating hysteresis in the tandem cell will be set out. The results of the simulations will be shown in Chapter 4. In this chapter the possible difference between single-junction and tandem behaviour will be investigated. Chapter 5 will offer an in-depth explanation of the possible difference between SJ and tandem behaviour and the entire hysteresis behaviour due to defects. Finally, this report will conclude with Chapter 6, where a summary will be given with the findings and recommendations will be given for future works.

2

Theory

To better understand the underlying physics of the tandem cell and the used models, important semiconductor physics will be explained in this chapter. First, the drift-diffusion model will be introduced in Section 2.1. After that, essential solar cell mechanisms will be explained, including recombination mechanisms (2.2) and defects (2.3). Section 2.4 will give additional information about tandem cell behaviour. The hysteresis behaviour has been introduced in Chapter 1, but in Section 2.5, a more detailed description of this phenomenon will be given.

2.1. Drift-diffusion model

The inner workings of a semiconductor, in this case a solar cell, are described by quantum mechanics theory. Modelling this would require titanic amounts of time and computational efforts, so instead the behaviour inside the cell will be modelled using a drift-diffusion model. Drift-diffusion models assume that the movement of charge carriers follow Newton's Laws and that properties of particles are dictated by quantum theory of solids. The theory described in this chapter is a summary of the works of Neamen [78] and Sze and Ng [79]. The models used are taken from the Sentaurus User Guide [80].

2.1.1. Energy states

From quantum mechanics follows that electrons from a single atom can occupy certain atomic orbitals. Only discrete energy levels for the electron are allowed. When this single-atom behaviour is applied to a crystal it is found that there are continuous allowed and forbidden energy bands throughout the crystal. The probability that an electron is occupying a certain quantum state with energy E is described by the Fermi-Dirac distribution:

$$f(E) = \frac{1}{1 + \exp(\frac{E - E_F}{kT})} \tag{2.1}$$

In this equation, E_F denotes the Fermi energy, k the Boltzmann constant and lastly T the temperature in Kelvin. Using Eq. 2.1, the number of electrons at each energy can be estimated. The highest band of electron energies in which electrons are normally present at absolute zero temperature is called the valence band, the band above this is called the conduction band. The range of forbidden energies between these two bands is called the bandgap, E_G. The energy levels of the conduction and valence band that border the bandgap are called the band edges and will be referenced by E_C and E_V.

2.1.2. Holes

Normally there are no electrons in the conduction band, but for T > 0K, an electron in the valence band may gain thermal energy and jump the bandgap leaving behind an empty spot. Mathematically, this movement can also be described by saying that an opposite charge went from the conduction band into the valence band. Since the valence band is close to entirely filled with electrons, modelling the empty states using this positive charge is evidently easier and computationally less work. This positive charge carrier is called a hole. This concept may be easier to understand when related to heat. Whenever

someone enters a room with a low temperature, they do not speak of a room that lacks heat, but of a cold room. The 'lack' of an electron being called a hole follows the same principle. The electron and hole charge carriers will be depicted by the letters n and p respectively from now on.

2.1.3. Quasi-Fermi levels

The Fermi energy is only defined in the case that the device is in equilibrium, when this is not the case, quasi-Fermi levels can be defined. For this thesis the quasi-Fermi levels are modeled using Fermi statistics, resulting in the following equations:

$$n = N_C \exp\left(\frac{E_{F,n} - E_C}{kT}\right) \tag{2.2}$$

$$p = N_V \exp\left(\frac{E_V - E_{F,p}}{kT}\right) \tag{2.3}$$

In these equations E_{Fn} and E_{Fp} are the quasi-Fermi levels, and N_C & N_V are the effective density-of-states of the conduction and valence bands respectively.

2.1.4. Energy-band diagrams

A common way to show semiconductor characteristics is an energy band diagram. In an energy band diagram, important energy levels within the device are shown as a function of the spatial position. Most importantly, a band diagram shows the E_C and E_V for all materials, and the E_F for the device. This helps to see which way the charge carriers will flow and what barriers may exist within the device. A simple energy-band diagram can be seen in Fig 2.1. The left-hand figure shows the band-diagram of a material under dark-conditions. The right-hand figure shows a band-diagram where the Fermi level is split into two quasi-Fermi levels due to either applied voltage and/or illumination [1].

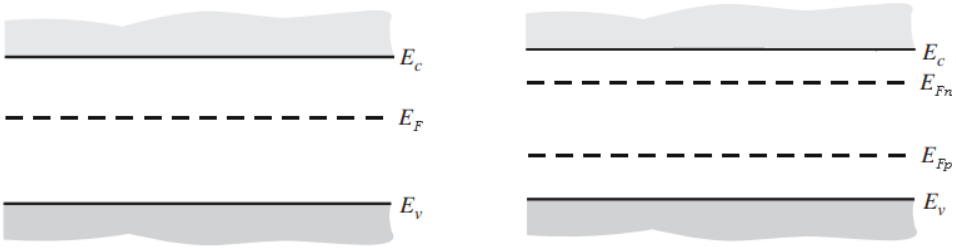

Figure 2.1: Two energy band-diagrams for a material under dark conditions (left), and one under applied voltage and/or illumination (right)

2.1.5. Trap states

So far the assumption was made that there are no possible energy states within the forbidden-energy bandgap. In a real semiconductor however, defects within the material can cause discrete energy states within the forbidden region. These defects, or traps, can act as a recombination center for both types of charge carriers. Traps can be of the acceptor or donor type. There are four kinds of basic trapping and emission processes, these processes can be seen in Figure 2.2 for an acceptor type trap.

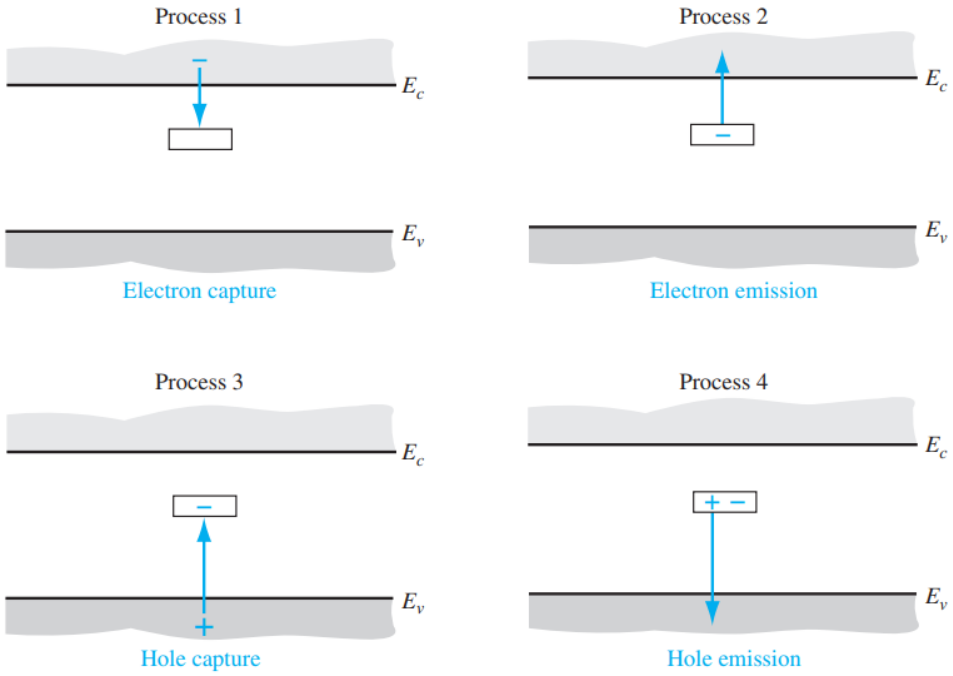

Figure 2.2: The four types of trapping and emission processes as shown in Neamen [78]

When the electron occupation f_t of a trap is denoted as either 0, for empty, or 1, for full, the value can be based on the four processes of trapping and emission. This results in the equation used to model trap behaviour in Sentaurus:

$$\frac{\partial f_t}{\partial t} = (1 - f_t)c_C^n - f_t e_C^n + (1 - f_t)c_V^n - f_t e_V^n \tag{2.4}$$

In which c_C^n and c_V^n are the capture rates from the conduction and valence band respectively, and e_C^n and e_V^n are the emission rates to both bands. It is important to note that a hole capture is the same as an electron emission as explained in 2.1.2. Because of this, c^n can be switched out for e^p and e^n for c^p. The emission and capture rates are modeled as shown in Eq. 2.5 and 2.6

$$c_C^n = \sigma_n v_{th}^n n \tag{2.5}$$

$$c_C^p = \sigma_p v_{th}^p p \tag{2.6}$$

With σ being the capture cross-section, v_{th} the thermal velocity, and n & p the electron and hole densities. The hole and electron capture cross-sections are measurements as to how likely it is that a defect captures an electron or hole.

The probability that an acceptor trap is occupied by an electron and has a negative charge, is given by

$$f(E_t) = \frac{1}{1 + \exp\left(\frac{E_t - E_F}{kT}\right)} \tag{2.7}$$

Since Sentaurus defines a filled donor trap as occupied when it has captured a hole and has a positive charge, the probability it is filled becomes

$$f(E_t) = \frac{1}{1 + \exp\left(\frac{E_F - E_t}{kT}\right)} \tag{2.8}$$

This means that, for an acceptor trap, when the energy of a trap is significantly under the Fermi level, the trap is almost always full. Vice versa, when the trap energy is significantly above the Fermi level, it is likely to be empty. This leads to a distribution that can be seen in Figure 2.3.

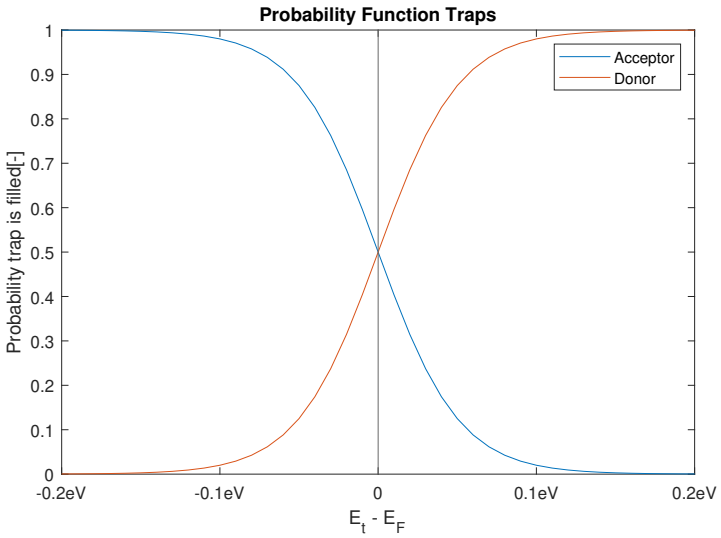

Figure 2.3: A band-diagram showing the likeliness of a trap to be filled based on how close it is to the Fermi level for 300K

When the fermi level is split into quasi-Fermi levels, the acceptor type traps are influenced by the hole quasi-Fermi level, E_{Fp}, whereas the donor type traps by the electron quasi-Fermi level, E_{Fn}.

2.2. Recombination mechanisms

There are multiple mechanisms by which electrons and holes can recombine unwanted. For this model, Shockley-Read-Hall (SRH), radiative recombination, and Auger recombination are the principal mechanisms. Out of the three, SRH is expected to be the most prominent, as it is related to the defects used to model hysteresis.

2.2.1. Shockley-Read-Hall

Trap states can act as recombination centers within the bandgap, meaning an electron and hole have a probability of recombining there. This recombination mechanism is important for materials with a lot of defects, in this case perovskite. The SRH recombination rate is implemented into Sentaurus with the following equations:

$$R_{SRH} = \frac{N_0 v_{th}^n v_{th}^p \sigma_n \sigma_p (np - n_i^2)}{v_{th}^n \sigma_n (n + n_1/g_n) + v_{th}^p \sigma_p (p + p_1/g_p)} \tag{2.9}$$

with:

$$n_1 = n_i \exp\left(\frac{E_{trap}}{kT}\right) \tag{2.10}$$

$$p_1 = n_i \exp\left(\frac{-E_{trap}}{kT}\right) \tag{2.11}$$

In these equations n_i is the intrinsic carrier concentration, n and p the electron and hole concentrations, g represents the degeneracy factor and E_{trap} is the difference between the defect level and the intrinsic level. The degeneracy factor is a measure of the number of defect states with the same energy level [81].

2.2.2. Radiative

This type of recombination happens mainly in direct bandgap semiconductors. A material has a direct bandgap when the crystal momentum of electrons and holes is similar in both conduction and valence band. This means that it can directly emit a photon, whereas in an indirect material, a photon first has to change its momentum by interacting with the lattice [1]. Perovskite happens to be a direct bandgap semiconductor, meaning this mechanism is important for this model. c-Si is considered an indirect bandgap material.

$$R_{dir} = \beta(np - n_i^2) \tag{2.12}$$

With β being the recombination coefficient.

2.2.3. Auger

Auger recombination can be important for direct bandgap materials with high doping concentrations. It is a three-particle process, either between an electron and a hole, transferring the energy to another free hole, or to a free electron. The third particle will dissipate its energy in the lattice as heat. The first process mainly occurs in p-type materials, and the second process with the free electron mainly in n-type materials.

$$R_{aug} = \left(C_n n + C_p p\right)\left(np - n_i^2\right) \tag{2.13}$$

With C_n and C_p being the temperature-dependent Auger coefficients.

2.3. Defects

Research has found defect states in perovskite [82, 83] and shown that these defects play a significant role in the physics of a perovskite absorber layer [84, 85]. The defects can be classified based on their energy levels as either deep or shallow defects. Shallow defects have their average energy level in the bandgap but near the edges, whereas deep defects have their average energy level more to the middle of the bandgap.

2.3.1. Defects in perovskite cells

Although this research is based on modelling defects, it is good to ground these assumptions in reality. Crystalline semiconductors can exhibit different types of defects. These defects can be categorized in two main categories. They either are interruptions to the normally perfect crystal lattice (crystallographic defects) or they are impurities (atoms that should not be there). Figure 2.4 shows these defect types.

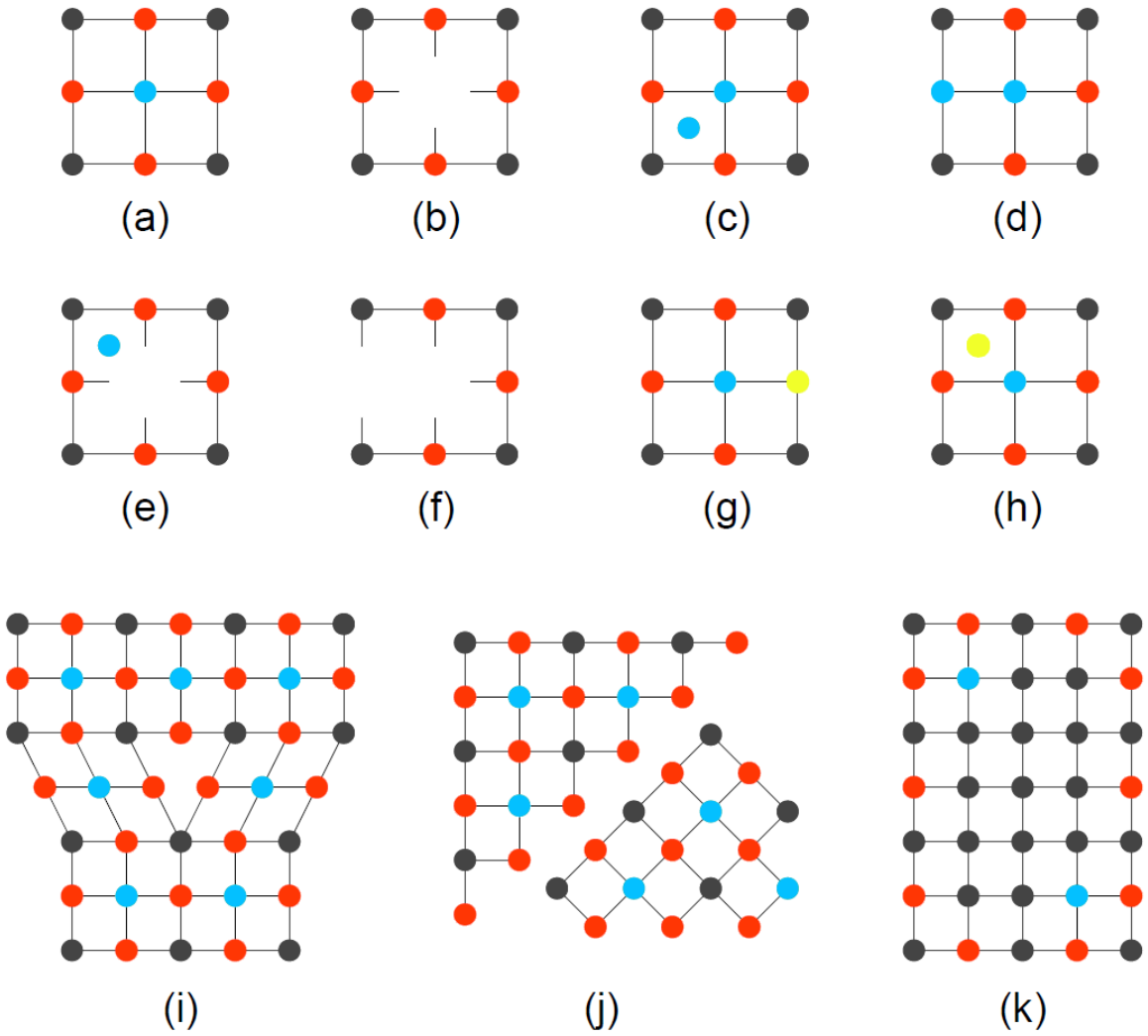

Figure 2.4: Illustration of point defects and higher-dimensional defects in a perovskite crystal lattice (blue, grey, and red dots represent the A-, B-, and X-site ions respectively, yellow dots represent foreign atoms). (a) perfect lattice, (b) vacancy, (c) interstitial, (d) anti-site substitution, (e) Frenkel defect (simultaneous interstitial and vacancy of the same ion), (f) Schottky defect (anion and cation vacancies occurring together), (g) substitutional impurity (h) interstitial impurity, (i) edge dislocation, (j) grain boundary, (k) precipitate. Reproduced from Ball and Petrozza [84]

2.3.2. Deep defects

It is suggested that deep defects are unlikely to form within MAPbI3 [85]. This was based on theoretical calculations showing these defects have high formation energies which should make them significantly less likely to form than shallow defects. However, interactions between lead cations and iodide anions have been shown to result in specific charge states with lowered formation energies. This makes it possible for deep defects to form [86].

2.3.3. Interface defects

Because the different materials used for the cell layers have deviating lattice structures, the number of deep defects is significantly higher near the interfaces as opposed to in the bulk. This was confirmed by Ni et al. [87] by using drive-level capacitance profiling. They found that the defect concentrations near the interfaces can be orders of magnitude higher than within the bulk, depending on layer materials used.

2.3.4. Band tail states

Structural disorder within absorber materials can result in localized energy states within the bandgap with energy levels slightly within the bandgap. These states are band tail states, or Urbach tails. Band

tail states have been found in many amorphous materials and have shown similar characteristics for each [88, 89, 90]. The defect concentrations for these tail states follow an exponential distribution with characteristic energies W_V and W_C, for the valence band and the conduction band respectively.

The Urbach energy seems to be a good representation for W_V and W_C, and can be found by taking the slope of the exponential absorptance curve. At standard conditions, MAPbI3 has shown Urbach energy values of around 15meV [91, 92].

2.4. Deeper insight into tandem cells

As mentioned before, when two absorber materials are stacked vertically, they are in tandem configuration. This way a broader part of the light spectrum can be absorbed in a more efficient manner, resulting in higher PCE's. There are multiple ways a tandem cell can be configured, but the type used for this case is a 2 terminal (2T) tandem cell, meaning there are two points for current collection: a bottom and a top contact. Other tandem architectures, 3T and 4T, can have more terminals as seen in Fig 2.5, commonly resulting in higher PCE's but also in very high fabrication costs making 2T most feasible.

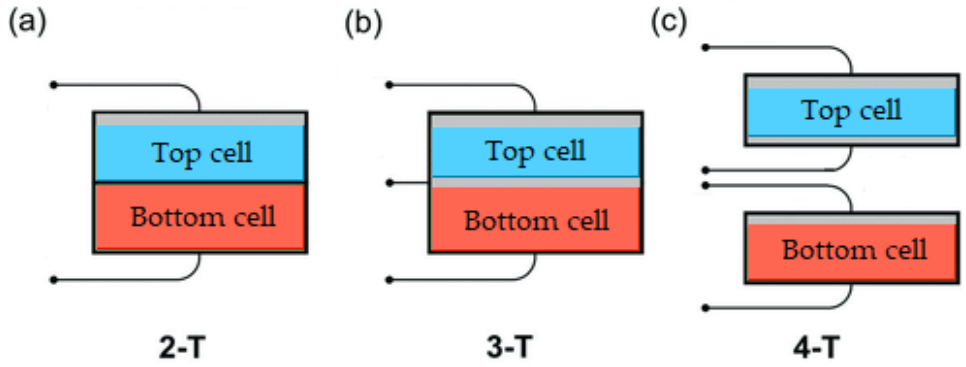

Figure 2.5: Three main tandem architectures

One of the most important constraints on a 2T tandem cell is that the current of both cells has to be the same. Because of this, even if one of the cells could produce more current, this energy is instead dissipated as heat. This means that both cells should convert the same amount of photons to electrons for maximum efficiency. The percentage of incident photons converted to electrons in a material per wavelength is described as the External Quantum Efficiency (EQE). To obtain optimal power conversion, the thickness of the absorber layers should be optimised, to ensure both of them generate the same current. Other ways to improve the power conversion are optical improvements such textured surfaces and reflective back contacts.

2.5. Hysteresis

As introduced in the first chapter, hysteresis is an important behaviour in perovskite devices. In this section a more detailed explanation will be given for this phenomenon.

It has been shown different conditions can influence hysteresis behaviour, including but not limited to light soaking, scan rate and applying a voltage bias before the reverse sweep [54]. Research has measured hysteresis behaviour with different scan rates. But these results take varying conclusions. Tress et al. [59] and Sanchez et al. [65] show more hysteresis behaviour at a scan rate of 1 V/s, Snaith et al. [51] for 0.044 V/s, and Messmer et al. [93] for scan rates lower than 0.1 V/s. Snaith et al. [51] finds more hysteresis when the scan rate is reduced from 0.3 V/s to 0.011 V/s, whereas Dualeh et al. [94] discovers less hysteresis when the scan rate is reduced from 0.2 V/s to 0.01 V/s. From these widely varying results, it should be gathered that the hysteresis behaviour is highly device dependent. Another interesting note is that, based on these findings, a device that seems hysteresis free can very well have very severe hysteresis for another scan rate.

2.5.1. Origin

As of the present, researchers have not found empirical evidence for what causes hysteresis in perovskite devices. Multiple possible origins have been proposed and will now be further elaborated on.

Ion migration

The main proposed mechanism responsible for hysteresis is ion migration. It has been observed that by applying an electric field across a perovskite cell, a self-sustained electric field is created as a result of ion migration towards the electrodes [55]. Research suggests that I^- ions migrate towards the HTL, whereas MA^+ ions towards the ETL under illumination. These ions would then advantageously screen the build-up of charge near the interfaces, improving the charge collection [51]. Calado et al. [95] argues that both ion migration and trap states are necessary mechanisms for hysteresis to occur. Even though this is the most common explanation, it can not fully explain the hysteresis behaviour. So it is expected some other mechanism plays a role.

Trap states

Because of the deposition methods of perovskite, large amounts of defects can occur near interfaces. As explained in 2.1.5, these defects can act as a recombination center. Literature also argues that these defects can cause hysteresis [62]. This is explained by suggesting that the defects trap charge carriers under forward bias conditions and release them under short-circuit conditions, resulting in the other term, trap states. This behaviour results in the creation and dismantling of interfacial charge. This would then give rise to hysteresis when comparing the J-V curve measured with reverse and forward bias. For this behaviour, the scan rate of the curves should heavily influence the amount of hysteresis. Since the trapping and de-trapping is a relatively slow mechanism, higher scan rates would not give the traps the opportunity to influence the measurement. This mechanism is the main explanation used to model hysteresis in this report.

Capacitive effects

Researches like Sanchez et al. [65] and Juarez-Perez et al. [66] have measured large displacement current in perovskite cells. They argued that these currents had been induced by capacitive effects. However, both trap states and ion migration have been shown to cause displacement currents, and the behaviour occurs in all types of semiconductor devices [63]. Tress et al. [59] explains that the hysteresis shown in perovskite cells would require a capacitance in the order of mF/cm^2 to be explained by capacitive effects, whereas geometric capacitance is in the order of $\mu F/cm^2$.

Ferroelectric polarization

A number of papers claim that the hysteresis behaviour is due to ferroelectric polarization [68, 69, 70]. Ferroelectric domains would be created under illumination at V_{OC} and these domains would aid in charge separation and reduce recombination. Coll et al. [96] has shown that these ferroelectric domains can only linger for small timescales, unlike the hysteresis effect that remains for lower scan rates and thus larger timescales. On top of that, inorganic $CsPbI_3$ has also displayed hysteresis [97], even though inorganic materials cannot show ferroelectric properties.

2.5.2. Hysteresis index

To objectively compare results, a quantitative value should be given to the hysteresis behaviour. For this case, the definition from Nemnes et al. [98], as used in Heerden et al. [63], is applied. In these works, the mechanism is quantified using a Hysteresis Index (HI), which is defined by the following equation:

$$HI = \frac{\int_0^{V_{OC,Rev}} J_{Rev}(V)dV - \int_0^{V_{OC,Forw}} J_{Forw}(V)dV}{\int_0^{V_{OC,Rev}} J_{Rev}(V)dV + \int_0^{V_{OC,Forw}} J_{Forw}(V)dV} \tag{2.14}$$

This equation integrates the current density over the voltage for both forward and reverse scans. A graphic explanation is given in Figure 2.6. The The possible values are -1 ≤ HI ≤ 1, with positive values showing normal hysteresis and negative values inverted. Larger values indicate stronger hysteresis

behaviour. It should be noted that the hysteresis index has no direct physical meaning, its main use is to be able to compare different simulations.

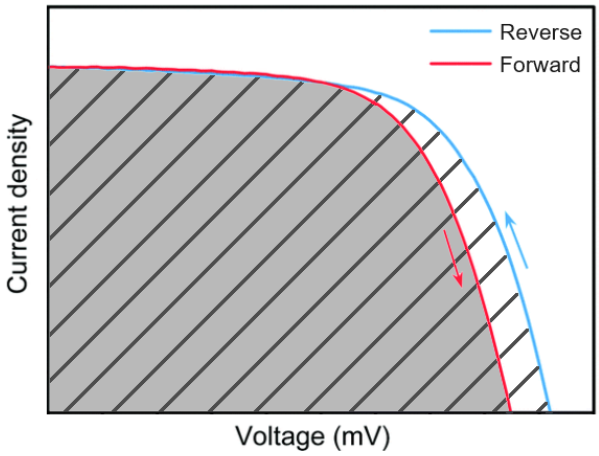

Figure 2.6: A graphic explanation of Eq. 2.14. The dashed area the integration depicts the integration of the reverse scan (left term in the equation), area in gray depicts the integration of the forward scan (right term in the equation)

3
Methodology

This chapter aims to develop a method to fulfill the first objective, to simulate hysteresis behaviour in a perovskite / c-Si tandem cell using defects. The solar cell model was made in a preliminary study, so this chapter focuses mostly on the methodology for the electrical simulation setup. In this chapter, Section 3.1 will go over the software used for this project. The tandem device architecture will be discussed in Section 3.2. The modelling of defects and recombination is explained in Sections 3.3 and 3.4. Lastly, Section 3.5 sets out the simulation process.

3.1. Simulation setup

The model is simulated in Synopsys Sentaurus. First, the model is subdivided into discrete geometric cells, or vertices. This operation is called meshing. Sentaurus generates this mesh and gives the possibility to refine the mesh locally. This step is necessary close to interfaces because larger gradients can occur here, making more vertices a necessity. Then optical, thermal, and electrical simulations can be performed for the device. For this case, the optical simulation is done using GenPro4, which will be explained further on. These simulations are done using a Newton-like solver to solve the semiconductor equations, as mentioned in Section A.1. To model the defect spatial densities, a C++ extension is used. Two types of simulations are used for this study. Transient simulations have a time aspect and are used to study the effect of different scan rates. The second type are quasi-stationary simulations. Here the device is assumed to be in steady state. After the simulations have been performed, they can be analysed. This can be done for a plethora of variables. Lastly, for a more in depth analysis, the extracted results can be brought into MATLAB.

3.1.1. Convergence

Simulations using Sentaurus have many benefits, they are relatively cheap and measurements are easy. However, these simulations are not limitless. The biggest hurdle to clear is convergence. To solve all the semiconductor equations for a given moment, they first are given an initial value, based on those values the next iteration is done until the resulting values do not significantly change when compared to the last iteration and thus become stable. This is what is referred to as convergence.

Convergence can be influenced in many ways, some of which are that the mesh can be refined or the time-step can be tweaked. This way more complex simulations can be made possible, but this can not be done infinitely. At a certain point the simulation just has too many variables and the results become divergent. For this research, the most limiting factor is the amount of defects and the complexity of the mesh. As more defects are added, it simply becomes too much for Sentaurus to compute. On top of that, the model is quite complex, resulting in reliable results, but making it harder to simulate. The consequence of this is that some variables regarding the defects have limiting values, above which, convergence could not be reached.

3.1.2. Optical simulation

The optical simulations for this cell are done using GenPro4 [77]. The solar cell is modelled as a multi-layer structure. For each of these layers, GenPro4 calculates the fraction of incident light absorbed. Based on these calculations, the implied photocurrent is computed. GenPro4 is implemented in Sentaurus using a Matlab extension. The optical modelling was done prior to this research. So although GenPro4 is used to find the generated photocurrent in each layer, the layer thickness and texturing are outside the scope.

3.2. Tandem device structure

The tandem cell structure is summarized in Table 3.1 for the top cell and 3.2 for the bottom cell. The structure is an in-house template supplied by the PVMD group of TU Delft. The perovskite used for this cell is $FA_{0.8}Cs_{0.2}PbI_{2.3}Br_{0.7}$ [99], a mixed halide. The ETL of the top cell consists of C60 and the HTL of 2PACz. Two other unmentioned layers have been used as well. The BCP layer acts as a buffer layer that reduces non-radiative recombination between the ETL and the ITO [100]. The MgF layer is used as a passivation layer to reduce the amount of defects in the physical cells and to reduce surface recombination losses between the ETL and the absorber layer [101, 102]. The top cell is used on its own to model the single-junction (SJ) cell.

Table 3.1: Material parameters for the top cell

	ITO	BCP	C60	MgF	$FA_{0.8}Cs_{0.2}PbI_{2.3}Br_{0.7}$	2PACz
t [nm]	70	5	5	1	485	2
ε_r	4	11.9	10	6	6.5	10
E_G [eV]	3.1	3.5	2.1	10.9	1.68	3.5
χ [eV]	4.9	e.7	3.9	0.45	3.9	1.8
N_C [cm^{-3}]	4.18×10^{18}	2.2×10^{18}	2×10^{18}	6.91×10^{18}	4.42×10^{17}	2×10^{18}
N_V [cm^{-3}]	1.7×10^{19}	1.8×10^{19}	2×10^{18}	2.54×10^{19}	8.47×10^{18}	2×10^{19}
N_D [cm^{-3}]	0	1×10^{20}	0	0	0	5×10^{19}
N_A [cm^{-3}]	1.28×10^{20}	0	8×10^{18}	0	0	0

The bottom cell consists of the TRJ, n-aSi as the ETL, c-Si as the absorber layer, p-aSi as the HTL and ITO as the back TCO. Between the carrier transport layers and the absorber layer are intrinsic hydrogenated amorphous silicon layers. These layers act as passivation layers [103].

Table 3.2: Material parameters for the bottom cell [104]

	TRJ	n-aSi	i-aSi:H	c-Si	i-aSi:H	p-aSi	ITO
t [nm]	6	5	6.5	280×10^3	9.15	11.67	100
ε_r	4	11.9	11.9	11.9	11.9	11.9	4
E_G [eV]	3.1	1.84	1.86	1.12	1.93	1.69	3.1
χ [eV]	4.9	3.9	3.9	4.05	3.9	3.9	4.9
N_C [cm^{-3}]	4×10^{18}	2×10^{20}	2×10^{20}	2.8×10^{19}	2×10^{20}	2×10^{20}	4×10^{18}
N_V [cm^{-3}]	1.7×10^{19}	2×10^{20}	2×10^{20}	2.6×10^{19}	2×10^{20}	2×10^{20}	1.7×10^{19}
N_D [cm^{-3}]	0	0	0	0	0	2×10^{20}	0
N_A [cm^{-3}]	5×10^{19}	2×10^{20}	0	2.3×10^{15}	0	0	1.28×10^{20}

3.3. Defect modelling

The defects are modelled using the *Trap* function of Sentaurus. In the model, two types of defects are defined: acceptor and donor defects. Acceptor defects are uncharged when empty and negatively charged when they are occupied by an electron. In contrast, donor defects are uncharged when they contain an electron and are positively charged when empty. ETL defects are modelled as acceptor-like and HTL defects as donor-like. Heerden et al. [63] found that the hysteresis behaviour is more pronounced in this way, Chapter 5 will dive deeper into the reasoning for this.

3.3.1. Urbach states

The Urbach states concentrations are modelled following the research done by Wager [88]. For this implementation, the conduction band mobility edge, E_{CME}, and the valence band mobility edge, E_{VME}, are introduced. The mobility edges separate the localised tail states from the extended states in the respective bands, as seen in the figure. Because of this, the band tail states are expected to have an influence on the V_{OC} since the tails decrease the band gap slightly.

The band tail states near the conduction band are modelled as acceptors, and those near the valence band as donors. The densities (in $cm^{-3}eV^{-1}$) for the conduction band tail states, g_{TC}, and the valence band tail states, g_{TV}, follow the following equations:

$$g_{TC} = \frac{1}{2\pi^2}\left(\frac{2m_e^*}{\hbar^2}\right)^{3/2}\sqrt{\frac{W_C}{2}}\cdot\exp\left(\frac{E-E_{CME}}{W_C}\right) \tag{3.1}$$

$$g_{TV} = \frac{1}{2\pi^2}\left(\frac{2m_e^*}{\hbar^2}\right)^{3/2}\sqrt{\frac{W_V}{2}}\cdot\exp\left(\frac{E_{VME}-E}{W_V}\right) \tag{3.2}$$

with $\hbar$ being Planck's constant and m_e^* the effective mass for the extended states beyond the mobility edge. The Urbach tail states follow a uniform spatial distribution. The exponential distribution in Eq. 3.1 and 3.2 are modelled with $E_{CME} = \frac{1}{2}W_C + E_C$ and $E_{VME} = E_V - \frac{1}{2}W_V$ following [88].

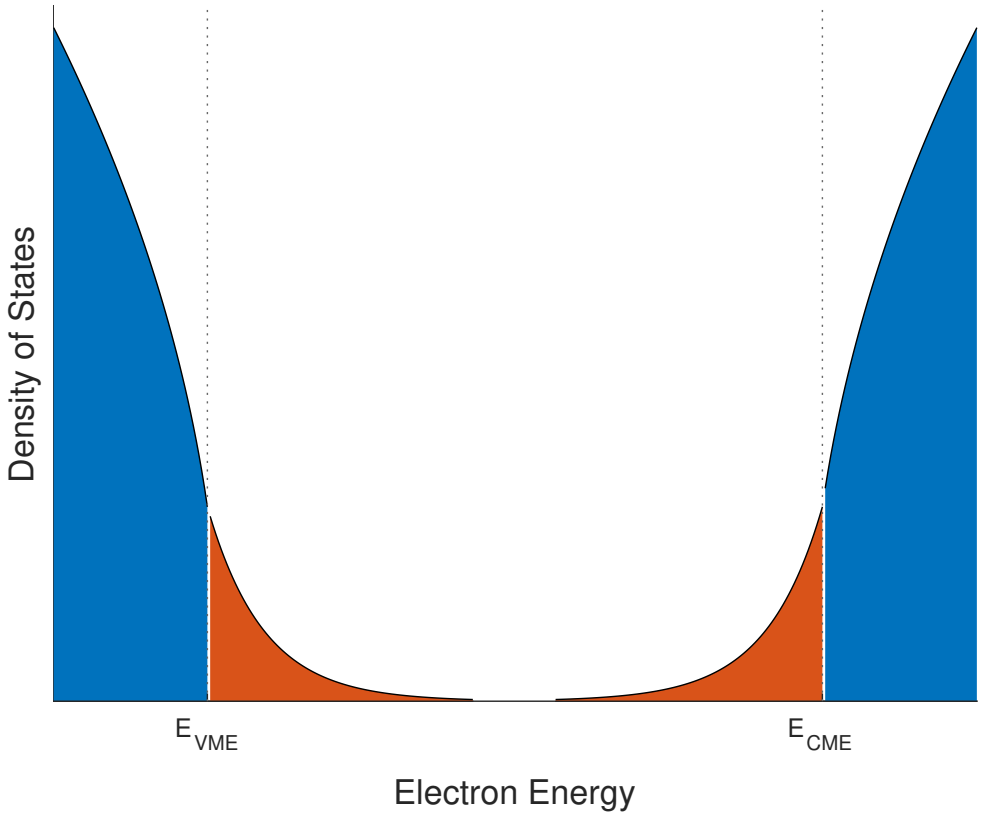

Figure 3.1: Density of States of Urbach tail states based on Eq 3.1 and 3.2. The tail states are shown in red. E_{VME} and E_{CME} are the valence band mobility edge and the conduction band mobility edge respectively. The characteristic energies are not to scale here, but exaggerated for clarity.

3.3.2. Deep defects

The interfacial defect concentrations are modelled using an exponential function, which decreases further from the interface. The concentrations of the interface defects at a certain position x within the

perovskite layer, are given by

$$N_t = N_{t,ETL}\exp\left(\frac{x_{ETL} - x}{\delta_{ETL}}\right) \tag{3.3}$$

for the ETL/perovskite interface and

$$N_t = N_{t,HTL}\exp\left(\frac{x - x_{HTL}}{\delta_{HTL}}\right) \tag{3.4}$$

for the perovskite/HTL interface. In these equations, $N_{t,ETL}$ and $N_{t,HTL}$ are the defect densities at the interfaces, x_{ETL} and x_{HTL} the respective positions of the interfaces, and δ_{ETL} and δ_{HTL} the penetration depths of the defects into the perovskite layer. The bulk defect concentration is uniform.
Research has shown that defect densities ranging from 10^{12} to 10^{17} [cm^{-3}] have been found near interfaces in perovskite [87]. With the bulk defect concentrations usually being 10 to 100 times lower. The effect of these defect densities will be discussed in Chapter 5. The default spatial defect distributions within the perovskite layer are shown in Fig 3.2. The defect densities shown in the figure are a lot higher than what was found in literature. These values were chosen based on initial tests to see what values would induce hysteresis.

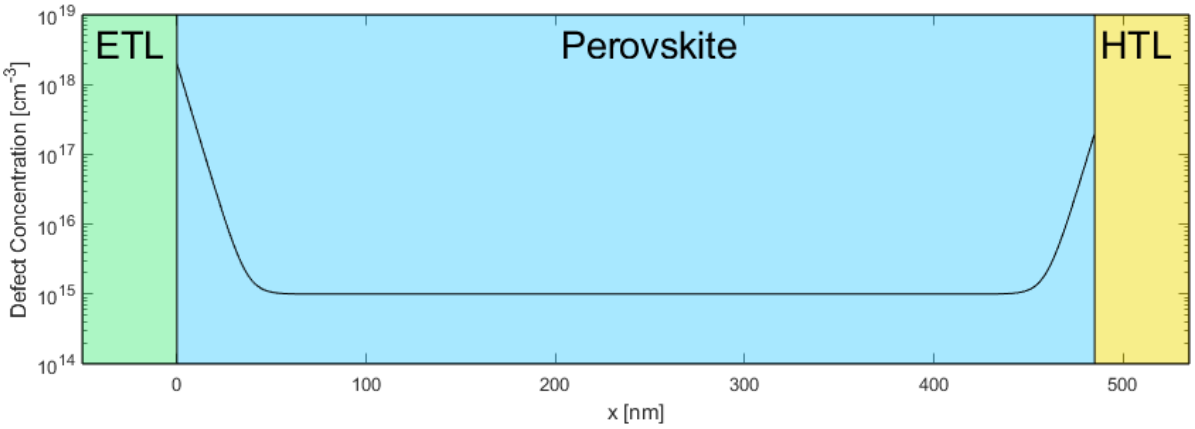

Figure 3.2: Modelled defect concentration within the perovskite layer.

On top of the defects having a distribution within space, they also have a distribution for their energy levels. Based on previous research the defects are modelled with Gaussian distribution [63, 82, 105].

$$N_t = N_{t,0}\exp\left(-\frac{(E - E_0)^2}{2E_\sigma^2}\right) \tag{3.5}$$

With $N_{t,0}$ being the trap concentration at that point in space, E_0 the average defect energy, and E_σ the standard deviation of the defect energy. The average defect energy near the ETL layer was set to 0.25eV, and near the HTL layer to 0.18eV. This was based on measurements from Duan et al. [82] and the simulation results discussed in Chapter 5. In that Chapter will also be explained why energy levels closer to the middle of the bandgap are not as important in the hysteresis behaviour.

Although the point of interest for this research is mainly the perovskite defects, the amorphous silicon layers in the bottom cell are also modelled with defects. This is using the values of Procel et al. [104] and is implemented to mimic a more realistic behaviour. The default defect parameters used for the perovskite layer are shown in Table 3.3. Unless stated otherwise, these values are used for the simulations. The values have been chosen based on preliminary simulation results showing hysteresis and on literature.

Table 3.3: Default parameters used for the perovskite defects

Parameter	Value	Unit	Description
$E_{t,ETL,0}$	0.25	[eV]	Average defect energy for ETL interface defects
$E_{t,HTL,0}$	0.18	[eV]	Average defect energy for HTL interface defects
E_σ	0.02	[eV]	Standard deviation of defect energy
$N_{t,ETL}$	2 x 10^{18}	[cm^{-3}/eV]	Defect concentration within perovskite at ETL interface
$N_{t,HTL}$	2 x 10^{17}	[cm^{-3}/eV]	Defect concentration within perovskite at HTL interface
$N_{t,bulk}$	1 x 10^{15}	[cm^{-3}/eV]	Bulk defect concentration
δ_{ETL}	0.01	[μm]	Penetration depth of ETL defects into perovskite layer
δ_{HTL}	0.01	[μm]	Penetration depth of HTL defects into perovskite layer
σ_n	1 x 10^{-23}	[cm^2]	Electron capture cross-section
σ_p	1 x 10^{-23}	[cm^2]	Hole capture cross-section
W_C	15	[meV]	Urbach energy at conduction band
W_V	15	[meV]	Urbach energy at valence band

3.4. Recombination models

For the perovskite absorber layer recombination models are implemented using the Sentaurus models mentioned in Section 2.2. The constants used for these models are listed in Table 3.4.

Table 3.4: Parameters used for Sentaurus recombination models for the perovskite layer

Parameter	Value	Unit	Description
β	2 x 10^{-10} [73]	[cm^3/s]	Radiative recombination coefficient
C_n	9.9 x 10^{-29} [10]	[cm^6/s]	Auger electron recombination coefficients (eeh)
C_p	9.9 x 10^{-29} [10]	[cm^6/s]	Auger hole recombination coefficients (ehh)

3.5. Transient simulation

The simulation starts off by applying a forward bias to the cell of V_{OC} using a quasi-stationary sweep, after which the light is turned on. Then the reverse scan is started as a transient simulation going to -0.2V. Then, without pausing, the forward scan is initialized which stops when V_{OC} is reached.

4

Results

In this chapter, the results of the simulations will be laid out. These will be used to reach the second objective, to find out if the tandem hysteresis behaviour differs from the single-junction. On top of that, the effect of different variables will be examined to understand where this possible deviation comes from. Unless mentioned otherwise, the simulations in this Chapter use the values stated in Table 3.3. Section 4.1 starts off by showing the effect interface defects have on the JV-curves of a perovskite / c-Si tandem cell and the single-junction cell. After this, Section 4.2 will show the effect of scan rate on JV-curves and will take a first look at the hysteresis index introduced in Section 2.5. The consequences of different capture cross-sections will be examined in Section 4.3. Section 4.4 will show the hysteresis plots for multiple defect densities. The effect of the Urbach energy will be displayed in Section 4.5. Since it was expected that the defect energy would have an impact on the hysteresis behaviour, the hysteresis index values for different defect energies were computed. These results can be seen in Section 4.6. The effect different architectures have on the hysteresis will be looked at in Section 4.7. Lastly, the developed model will be compared to other models and measurements of physical cells in Section 4.8.

4.1. Effect of interface defects

Based on literature, it is expected that simulations with higher defect densities near the interfaces of the perovskite will result in more hysteresis. Figure 4.1 shows the JV-curves for different defect distributions. All plots used a scan rate of 0.1 V/s. The non-defect case is shown in Figure 4.1a. It can be seen that the single-junction (SJ) curve has a higher J_{SC}, this means that the bottom cell in the tandem cell is current-limiting. The effect of ETL defects can be seen in Figure 4.1b. Here, the defect concentration is $2 \times 10^{18} cm^{-3}$, with the distribution as explained in 3.3. The defects are acceptor-like with an average energy level of 0.25eV from the valence band, these choices will be further explained in Section 4.6. For this figure, it can be seen hysteresis is present. The reverse scan remains unaffected while the forward scan shows significant losses at maximum power point. Figure 4.1c shows the curve for the same defect density, $2 \times 10^{18} cm^{-3}$, but at the HTL interface. For this case, the defects are donor-like with an average energy level of 0.18eV from the conduction band. For the same defect density, the hysteresis is way higher than for the ETL defects. It can also be seen that the reverse scan is also affected when compared to the no-defects JV-curve.

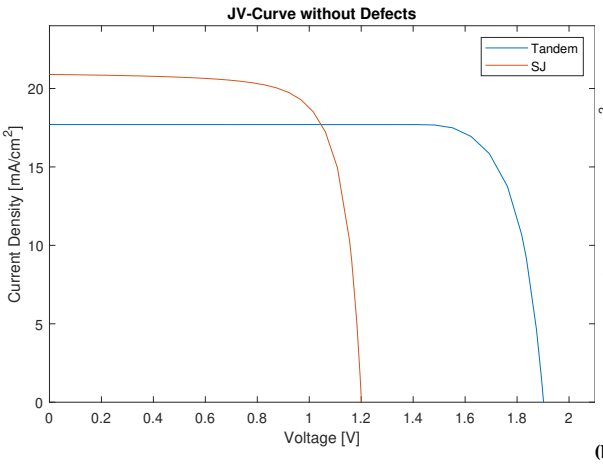

(a) JV-Curve of the device without perovskite defects

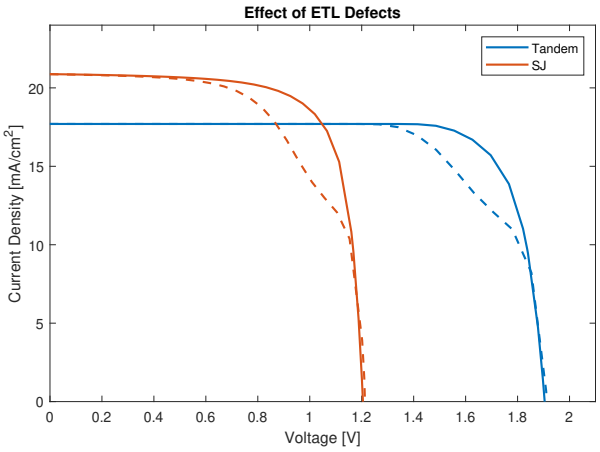

(b) JV-Curve with only ETL defects with a concentration of $2 \times 10^{18} cm^{-3}$ with the reverse scan with solid lines and forward with dashed

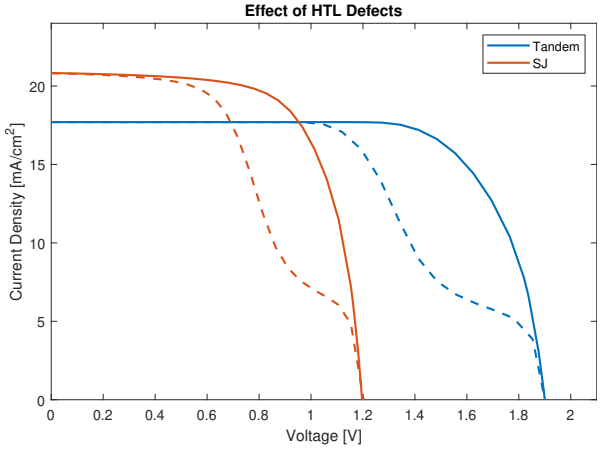

(c) JV-Curve with only HTL Defects with a concentration of $2 \times 10^{18} cm^{-3}$ with the reverse scan with solid lines and forward with dashed

Figure 4.1: JV-curves for multiple defect types and densities

4.2. Current-voltage curves

Since literature concluded that the scan rate has a big impact on the amount of hysteresis measured, JV-curves for different scan rates were plotted. As can be seen in Figure 4.2, the scan rate (sr in the figure) has indeed a big impact on the hysteresis behaviour. For these simulations ETL defects were used with a density of $3 \times 10^{18} cm^{-3}$. This was done to create a more pronounced hysteresis effect so the effect of the scan rate would be more evident. For a faster scan rate of 1 V/s, the hysteresis behaviour is quite modest. On the other hand, a scan rate of 0.1 V/s shows significant hysteresis for both SJ and tandem cells. Furthermore, for a slower scan rate of 0.01 V/s, both the forward and the reverse curves are affected, resulting in less hysteresis.

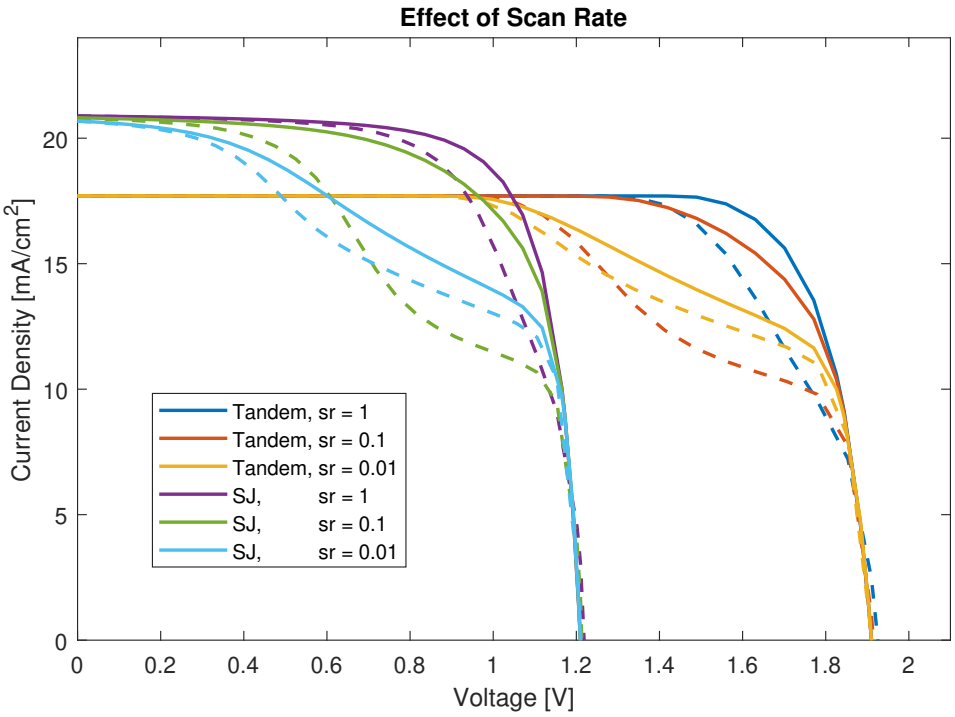

Figure 4.2: JV-curves for multiple scan rates in V/s with the reverse scan with solid lines and forward with dashed

The HI was simulated for more scan rates, for the same model, and plotted in Figure 4.3. Here, a distinct peak can be seen for 0.1 V/s. The figure shows a low HI for both sides of the peak, but the JV-curves of both sides differ immensely. The tandem cell shows a great increase in hysteresis for faster scan rates, higher than 10 V/s. This is likely caused by the defects in the silicon bottom cell layers, since Herman et al. [106] found hysteresis behaviour in silicon solar cells for scanrates higher than 15 V/s. More on this in Section 5.6.

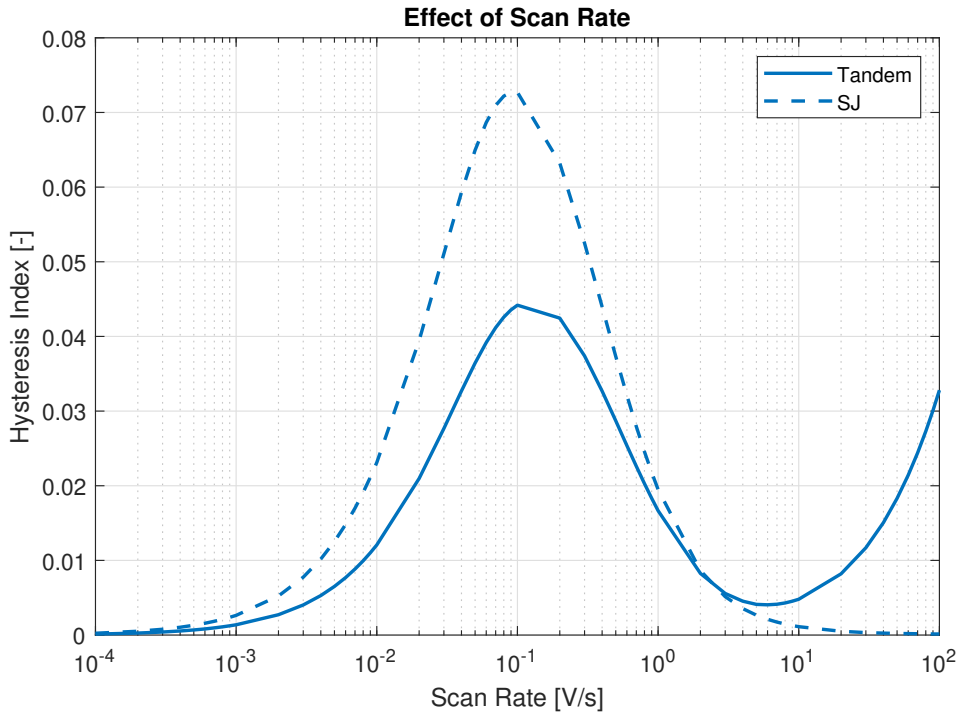

Figure 4.3: Hysteresis plot showing the effect of different scan rates

4.3. Capture cross-sections

In Section 2.1 it is explained that the capture cross-section is a measure of how likely a defect is to trap a charge carrier. It is expected that this has a effect on the hysteresis behaviour. To verify this, Figure 4.4 shows the tandem and SJ hysteresis plots for different capture cross-sections. It can be seen that when the capture cross-section is increased by a factor of 10, the scan rate for the peak of the hysteresis plot also increases by a factor of 10.

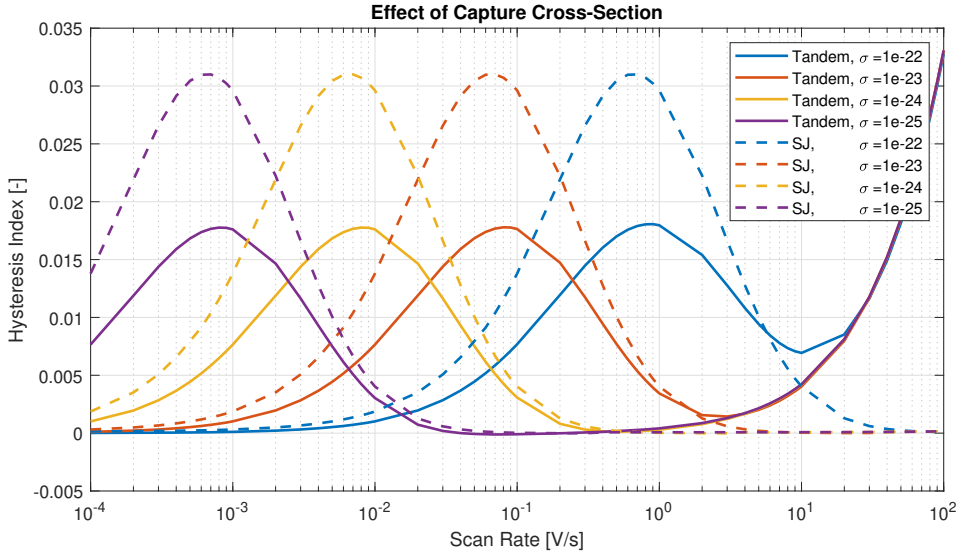

Figure 4.4: Hysteresis plot for both SJ and tandem device for multiple capture cross-sections in in $cm2$

4.4. Defects densities

It is expected that the defect density will have a huge impact on the amount of hysteresis in the modelled cell. In this section, multiple types of defects have been plotted with different concentrations.

The defects near the ETL interface have been modelled with defect densities of 0, 2×10^{18}, and 3×10^{18} cm^{-3}. The defects were also modelled with a density of 1×10^{18}, but this resulted in the same graph as for zero defects. The effect of a higher defect density seems to have a bigger impact on the SJ as was seen in the previous figures. It can also be seen that the peaks shift to the right for higher defect densities. The capture cross-sections were the same for these simulations, so the density alone has to have an effect on the optimal scan rate for hysteresis. The HTL interface defects were modelled with defect densities of 0, 1×10^{18}, and 2×10^{18} cm^{-3}. These values are a step lower than the ETL defects, which is because of convergence. It should be noted that, the HTL defects with a concentration of 2×10^{18} cm^{-3}, show much more hysteresis behaviour than the same defect concentration near the ETL layer. Also, the ratio between the the SJ and tandem is interesting. The difference between the two is much smaller than for the ETL defects. On top of that, for the HTL defects, the ratio seems to increase for higher defects much more visibly.

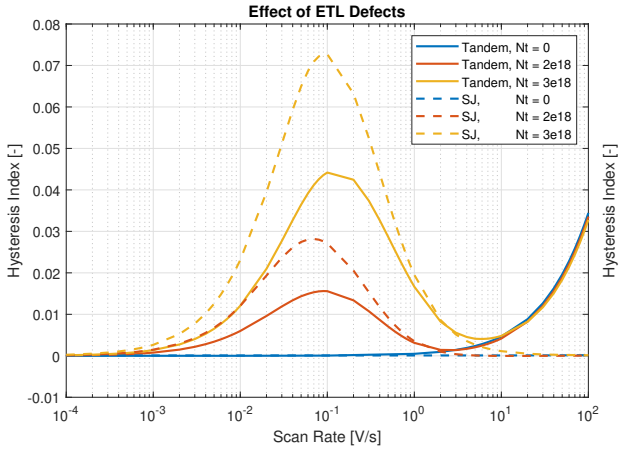

Figure 4.5: Hysteresis plot for both SJ and tandem device for multiple ETL defect concentrations in cm^{-3}

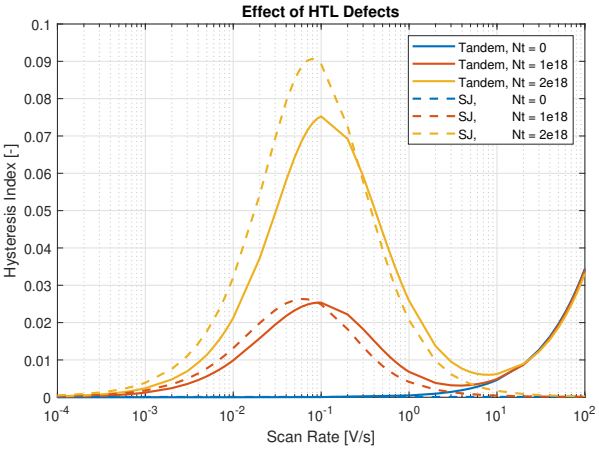

Figure 4.6: Hysteresis plot for both SJ and tandem device for multiple HTL defect concentrations in cm^{-3}

It becomes evident that the higher defect densities, result in a higher hysteresis index. This is expected, as more defects mean more charge can be stored, the driving force behind hysteresis. To put these results into perspective, the JV-curves for multiple defect concentrations are shown in Figure 4.7 and 4.8.

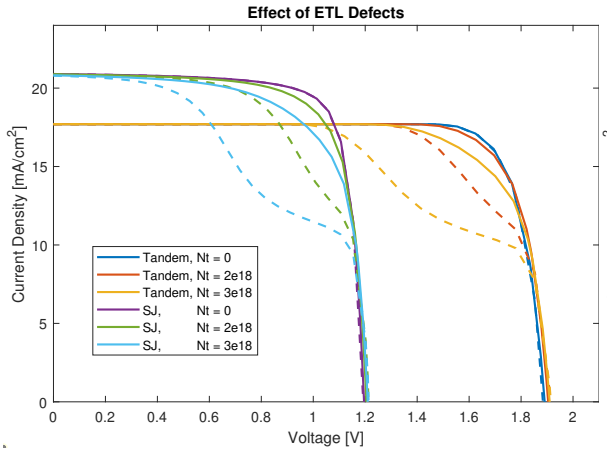

Figure 4.7: JV-curves for both SJ and tandem device for multiple ETL defect concentrations in cm^{-3} with the reverse scan with solid lines and forward with dashed

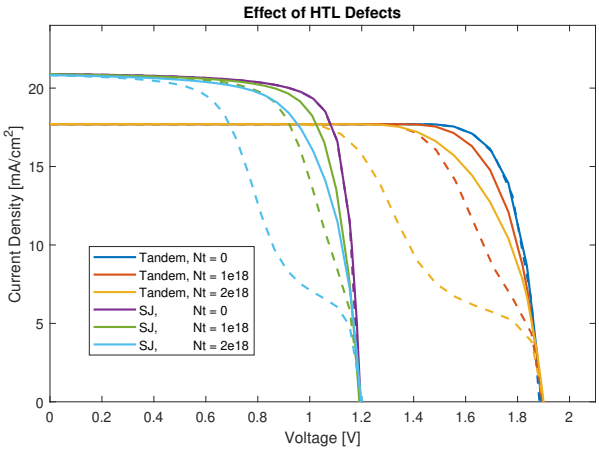

Figure 4.8: JV-curves for both SJ and tandem device for multiple HTL defect concentrations in cm^{-3} with the reverse scan with solid lines and forward with dashed

From these figures, it can be gathered that the defect density does not influence at what point the forward scan returns back to normal operations (the lower shoulder of the curve). But it does influence

at what point the hysteresis behaviour starts during the forward scan (the upper shoulder), shifting it further to the left for higher densities. It also brings the shoulder of the reverse sweep further left.

4.5. Urbach tail states

To investigate the effect of Urbach tail states, hysteresis plots for different Urbach energies were made. In Figure 4.9 it can be seen that there is a small increase in hysteresis index for Urbach energies of 15-25meV, but higher energies lead to less hysteresis. This can be explained by reviewing the model in 3.3.1. Although the density increases for higher Urbach energies, the average energy goes further into the conduction and valence bands, resulting in lower densities within the band gap. Although these Urbach tail states seem to have an effect on the hysteresis behaviour, the effect is very small. De Wolf et al. [91] found that for mixed halides, the Urbach energy is around 15meV. Based on this research and the outcomes of Figure 4.9, it is argued that Urbach tail states are not responsible for the large amounts of hysteresis found in perovskite cells.

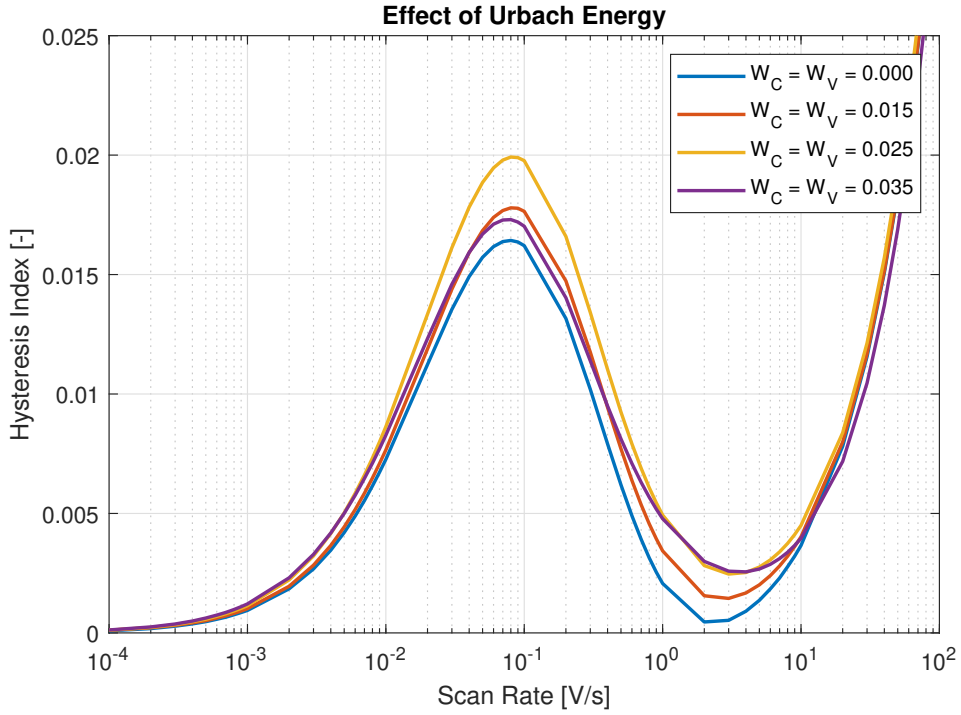

Figure 4.9: Hysteresis plot for both SJ and tandem device for multiple Urbach energies in eV

Since it was expected in Section 3.3.1 that the Urbach states would have an effect on the V_{OC}, these values were checked and the results can be seen in Table 4.1. It can be seen that for higher Urbach Energies, the V_{OC} decreases, as expected. The forward and reverse open-circuit voltage are the same for these cases.

Table 4.1: The reverse scan open-circuit voltage for different Urbach energies

W_C, W_V [meV]	$V_{OC,Rev}$ [V]
0	1.9115
5	1.9104
10	1.9080
15	1.9030
25	1.8810
35	1.8307

4.6. Defect energy

Although not all defect energies can be present in physical cells because they are coupled with existing defects types mentioned in 2.3, examining what energies could induce hysteresis could still be fruitful. Figures 4.10 and 4.11 show the hysteresis indices for different energy levels. The energies on the x-axis are compared to the energy level of the valence band. The defect densities for these plots are 2×10^{18} cm^{-3} at the interfaces.

It can be seen that the hysteresis behaviour has a peak for certain energy level, which is related to the quasi-Fermi levels as will be shown in Chapter 5. As the energy levels go towards the valence and conduction band (0eV and 1.68eV respectively), the hysteresis index goes to zero. The energy levels closer to the middle of the bandgap have not been simulated because of two reasons. The first reason is that these values are harder to simulate and not likely to reach convergence. The second reason, is that these values are not expected to induce hysteresis behaviour. It should be noted that the peaks for the ETL defects are 0.24eV for the tandem and 0.23eV for the SJ. The HTL defects resulted in the peak at 1.5eV for the tandem and at 1.51eV for the SJ, or at 0.18eV and at 0.17eV when compared to the conduction band at $E_C = 1.68$eV.

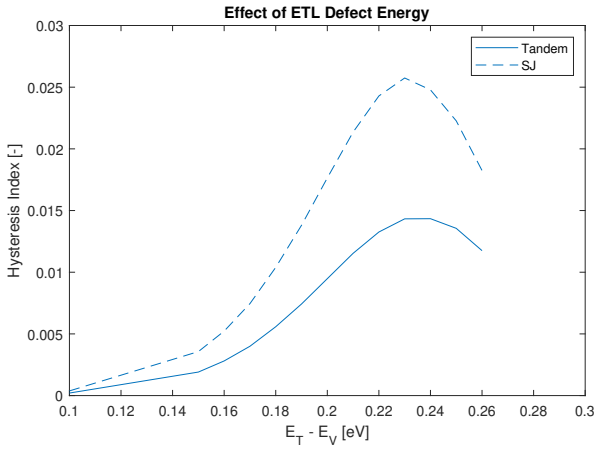

Figure 4.10: Hysteresis Index for different ETL defect energies

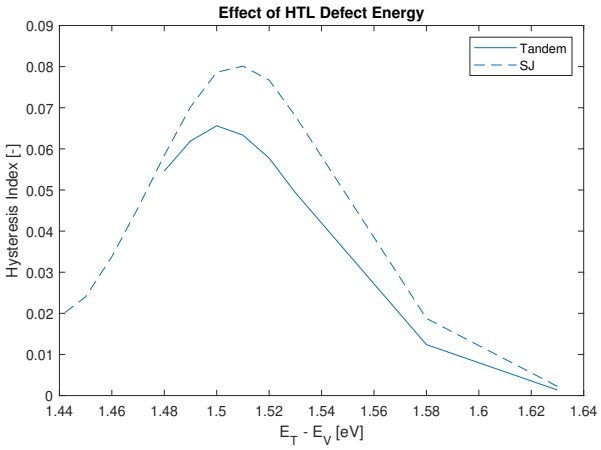

Figure 4.11: Hysteresis Index for different HTL defect energies

The effect the defect energies have on the JV-curves can be seen in 4.12. This plot shows the effect of traps near the ETL with a density of 2×10^{18} cm^{-3}. For trap energies of 0.26eV, it can be seen both the reverse and forward scans perform better than for the 0.24eV traps. The 0.24eV traps have the highest amount of hysteresis as shown in Fig 4.10. The traps with an energy of 0.2eV show less hysteresis because the reverse scan is affected more than the 0.24eV case, whereas the forward scan is only slightly worse. This behaviour seems to be similar for both the SJ as the tandem cell.

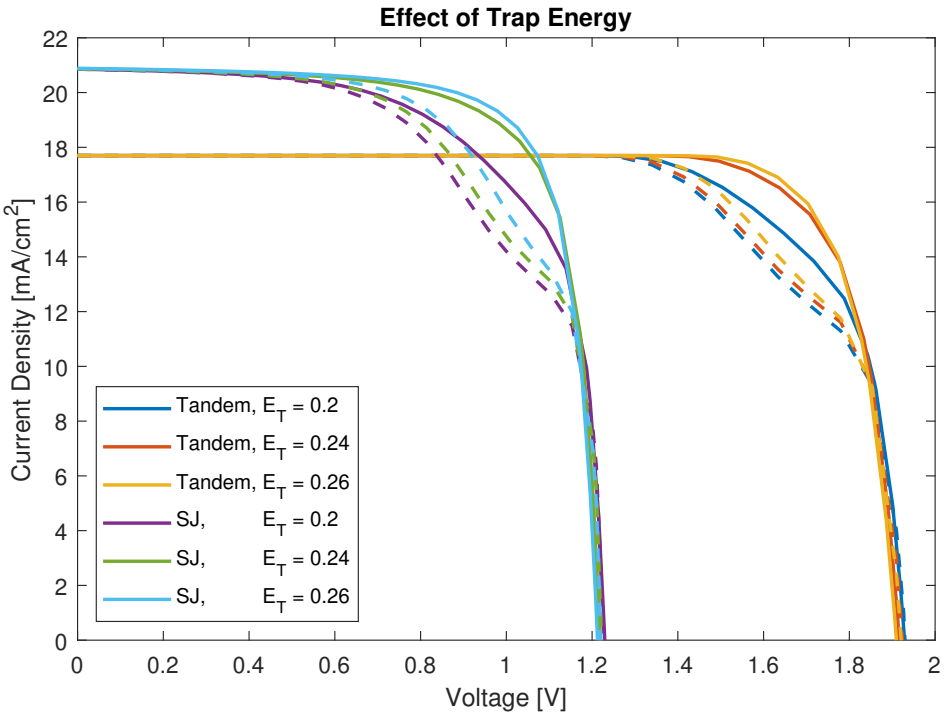

Figure 4.12: JV-curves for both SJ and tandem devices for multiple ETL defect energies in eV with the reverse scan with solid lines and forward with dashed

The HTL energy plot was also computed for different defect densities. This was done to verify the defect density does not influence at what energy level the peak hysteresis is found. The defect densities are 5×10^{17} and 2×10^{18} cm^{-3}. The results are found in Figure 4.13.

From this figure, it becomes evident that the defect density does not influence at what energy level the peak hysteresis is found. The tandem peaks are still found at 1.5eV and the single-junction peaks still at 1.51eV. Just as in previous figures, it can be seen that a higher defect density has a bigger impact on the hysteresis in the single-junction when compared to the tandem behaviour.

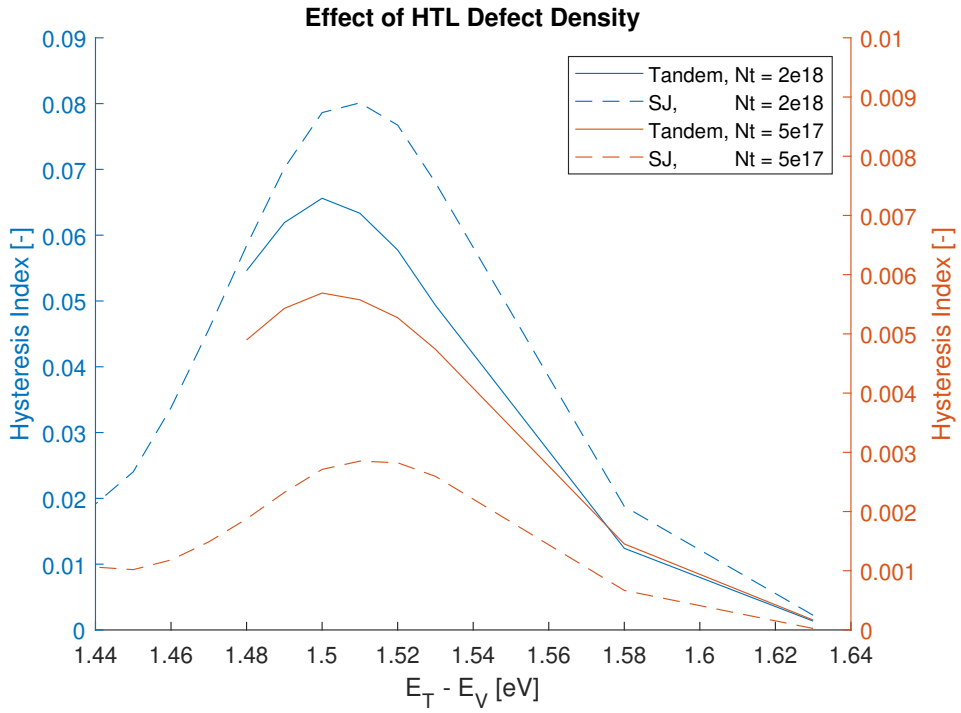

Figure 4.13: Hysteresis Index for HTL defect energies, with a defect density of 2×10^{18} cm^{-3} for the left axis (blue) and 5×10^{17} cm^{-3} for the right axis (red)

4.7. Effect of architecture

In the previous sections it became clear, the SJ and tandem behaviours are not completely similar. In almost all cases the SJ hysteresis index was higher for the same simulation inputs. To better bring out these differences, the JV-curves were plotted again with the voltage normalized. This can be seen in Figure 4.14 for ETL defects and in Figure 4.15 for HTL defects, both with a defect density of 2×10^{18} at the interface.

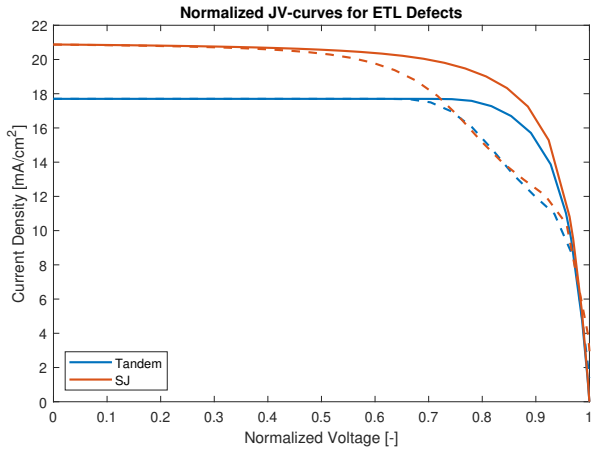

Figure 4.14: Normalized JV-curves for ETL Defects with the reverse scan with solid lines and forward with dashed

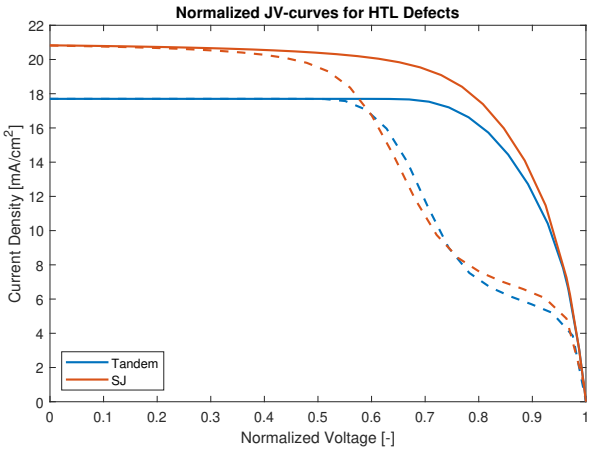

Figure 4.15: Normalized JV-curves for HTL Defects with the reverse scan with solid lines and forward with dashed

For both HTL and ETL, it can be seen that the difference between the forward scans is very minimal, it is mostly the reverse scan that is affected. This is expected to be because of the current-limiting c-Si cell. The small differences in the forward scan and the current-limiting will be investigated in Chapter 5.

4.8. Validation

To verify the tandem cell behaves realistically, it should be compared to existing models and measurements. Messmer et al. [93] uses a ion migration model to model a perovskite / c-Si tandem cell and compares this to the measurements of a similar physical cell made by Oxford PV. In this work, the hysteresis index is not used, instead the forward and reverse scan are compared by looking at the normalized fill factor. The reproduced data can be seen in Figure 4.16

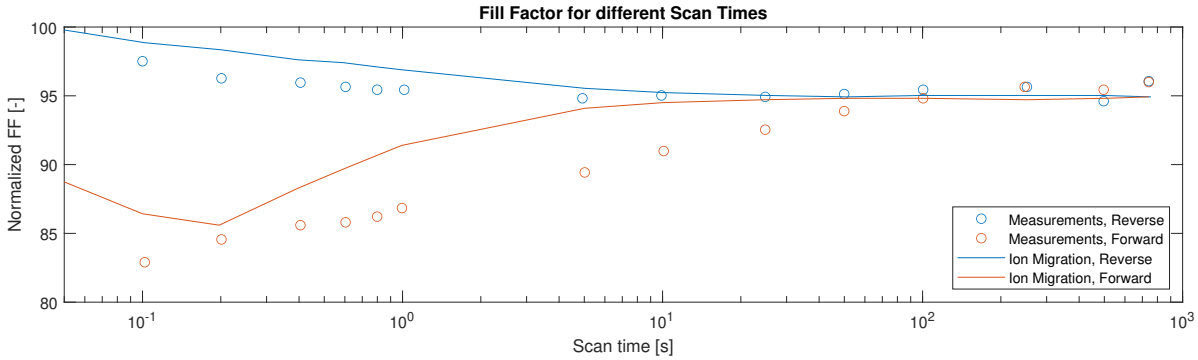

Figure 4.16: FF behaviour for an ion migration model and measurements, reproduced from [93]

It can be seen the general trend of the ion migration model used follows the measurements, although not by exact value. The most interesting part from the ion migration is the kink around 0.2s. To compare the developed tandem model to the data from Messmer et al. [93], the data from the simulations shown in 4.5 was taken for a defect density of 3×10^{18} at the ETL interface and put in the same format. Figure 4.17 shows the result.

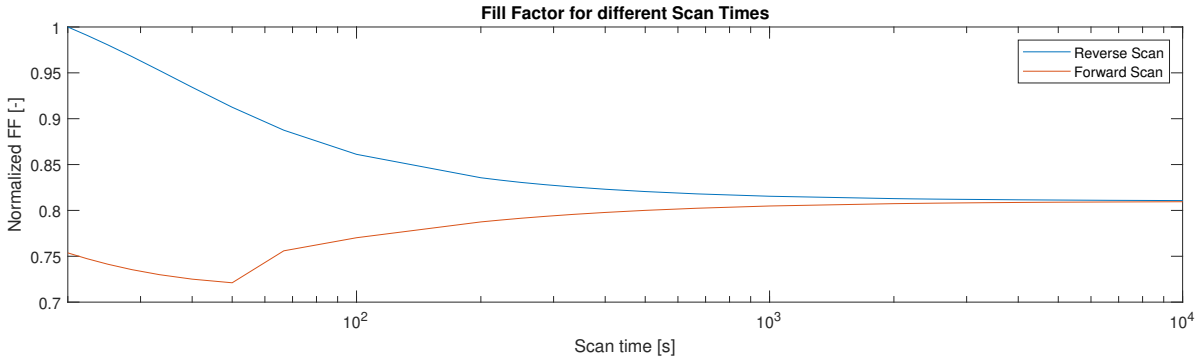

Figure 4.17: FF behaviour for tandem cell with defect density of 3×10^{18} at ETL interface

It can be seen that this model shows the same shape as the ion migration model. The overall performance seems to degrade faster which is understandable given that more defects are present. These defects are mostly active for longer scan times. Based on the previous findings, it is found the kink corresponds to the peak of the HI in Figure 4.5, so this is expected to be true for the ion migration model as well. Other than the difference in performance, the biggest difference between the two models and the measurements is that the developed hysteresis model displays this behaviour for larger scan times, meaning the hysteresis is slower than for measurements and the ion migration model. This could easily be calibrated by changing the capture cross-section of the model.

The point where the developed hysteresis model differs most from literature, is in the kink found in the forward scan when nearing V_{OC} when looking at the JV-curves. Most measurements find a decrease in performance around the maximum power point, just as for the model, but also a decrease in V_{OC}. In the models case, the V_{OC} stays roughly at the same value, since the forward scan resumes the behaviour

of the reverse scan after a kink for a certain voltage. This kink will be further investigated in Chapter 5. Some cases of the found kink have been found in literature, but these cases are sparse [107, 59]. Kang and Park [108] shows measurements for multiple cell types, some of which show hysteresis while keeping the V_{OC} and I_{SC} at the same point for reverse and forward scans. This implies that the hysteresis behaviour differs greatly for different cell architectures.

4.9. Conclusion

This chapter presented the results from the simulations to reach the second objective. To find out if the tandem cell behaviour differs from the single-junction cell. The second part of that objective, why it differs, will be explained in the next chapter. Additionally, the effect of changing different variables was shown. The defect densities affect the amount of hysteresis. The capture cross-section influences for which scan rate the hysteresis index peaks. It was shown the Urbach states are not likely to be responsible for large amount of hysteresis, they can, however, influence the open circuit voltage significantly. The energy level of the defects seemed to highly influence the amount of hysteresis. Most importantly, for all the previously mentioned variables, the tandem and single-junction hysteresis behaviour was shown to be similar but not equal.

On top of that, this chapter compared the developed model to other models and measurements. Although the exact values differ, which is understandable since the cell types were different for most datasets, the trends seemed to agree. With measurement data for this specific type of cell, the model could be calibrated and reach more realistic behaviour.

5
Discussion

This chapter will analyse the results found in Chapter 4 and discuss them based on the underlying theory. The objective of this chapter is to explain the deviation between tandem and single-junction cells shown in Chapter 4, and to explain the hysteresis behaviour as a result of defects. Section 5.1 will delve deeper into the mechanisms causing the hysteresis. The effect of the scan rate and the defect energy on the hysteresis behaviour will be investigated in Sections 5.2 and 5.3. Section 4.4 will look into how the defect density affects hysteresis. The difference in hysteresis behaviour between tandem and SJ cells is going to be looked at in Section 5.5. Section 5.6 will give a short insight into the defects in the bottom cell of the tandem. Lastly, Section 5.7 discusses the choice between modelling of hysteresis using ion migration and using defects.

5.1. Trap filling and emptying

To start off the chapter, the filling and emptying of the traps will be researched, to better understand what is happening in the perovskite layer. This will be done by looking at the different mechanisms taking place near the interfaces and in the layer and what consequences these have.

5.1.1. ETL interface defects

First, the defects near the ETL interface will be looked at. For these simulations, a defect density of $2 \times 10^{18} cm^{-3}$ at the interface was used. Based on the outcomes of Section 4.6, a defect energy of 0.24eV was used, and to better analyse the effect of a specific energy level, a uniform energy distribution was used. Furthermore a scan rate of 0.1V/s is applied. These variables result in the JV-curve shown in Fig 5.1. Because we expect a change of the quasi-Fermi level during the scan, it has been plotted out in Figure 5.2 for the voltages marked in the JV-curve. The trap energy is shown using a line at $E_{Fp} - E_V = 0.24eV$.

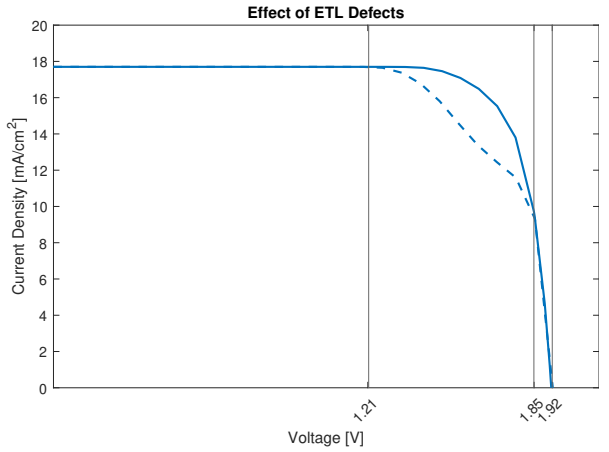

Figure 5.1: JV-curves for ETL defects with three voltage points marked for Fig 5.2

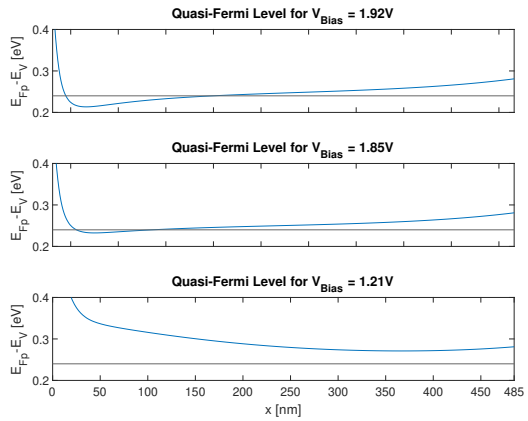

Figure 5.2: Quasi-Fermi levels for the voltages marked in Figure 5.1 during the reverse scan with the trap energy marked at 0.24eV

As can be seen, the quasi-Fermi level changes drastically near the interface. First it is below the trap energy for certain positions, indicating a low probability the traps are filled based on Figure 2.3. Later in the scan, the the quasi-Fermi energy is above the trap energy level for all positions, which would mean almost all traps are filled. Figure 5.3 shows the number of filled traps during this reverse scan for three voltage points. For V_{OC}, a voltage near V_{mpp} of 1.5V and a reverse bias voltage of -0.2V. In this plot a vertical line is shown at x = 12nm (or x = 3.093μm when considering the entire architecture of the cell). This point indicates the position at which the trap concentration changes most significantly, being a consequence of the quasi-Fermi level changing and of the trap spatial distribution. For this point, the number of filled traps is shown during the reverse scan and the forward scan in Figure 5.4.

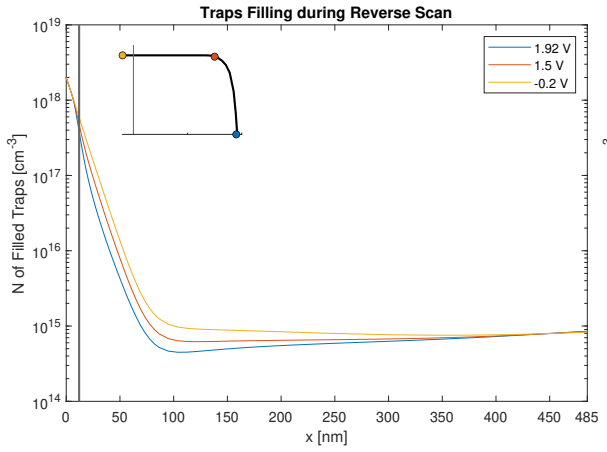

Figure 5.3: Concentration of filled traps in the perovskite layer for three voltages

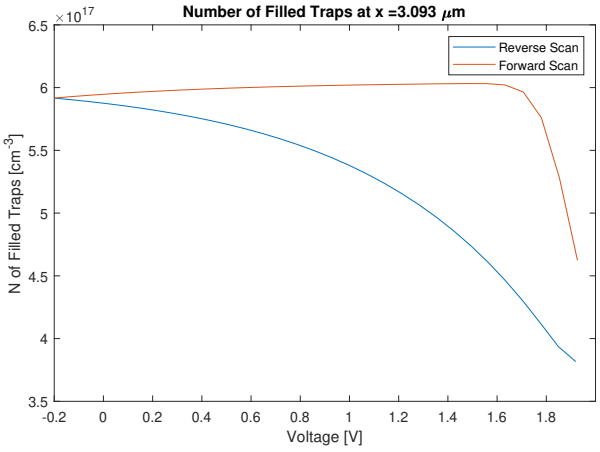

Figure 5.4: Concentration of filled traps at x = 3.093 μm (or 12nm into the perovskite layer from the ETL interface)

Figure 5.4 makes it evident the traps keep filling at this point during the reverse scan and most of the forward scan, until a certain point is reached where they start emptying again. Using Eq 3.3, it is calculated that the total number of traps at this point is approximately $6 \times 10^{17} cm^{-3}$. This means that at the start of the reverse scan the percentage of filled traps is roughly 62%. Which according to Eq. 2.7 means the quasi-Fermi level should be slightly above the trap energy. This can be verified by looking at the quasi-Fermi level for this position during the simulation in Figure 5.5.

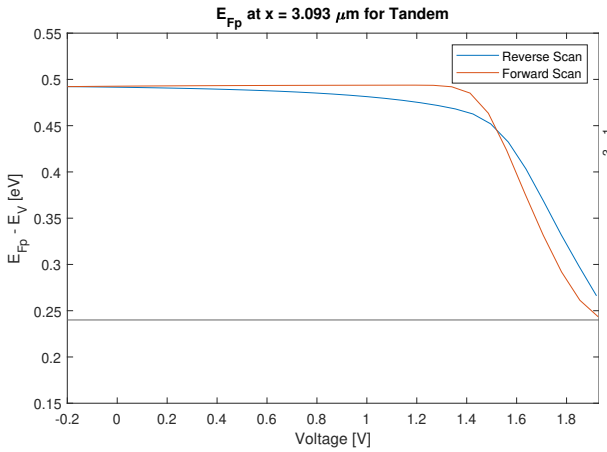

Figure 5.5: Quasi-Fermi level at x = 3.093 μm (or 12nm into the perovskite layer from the ETL interface)

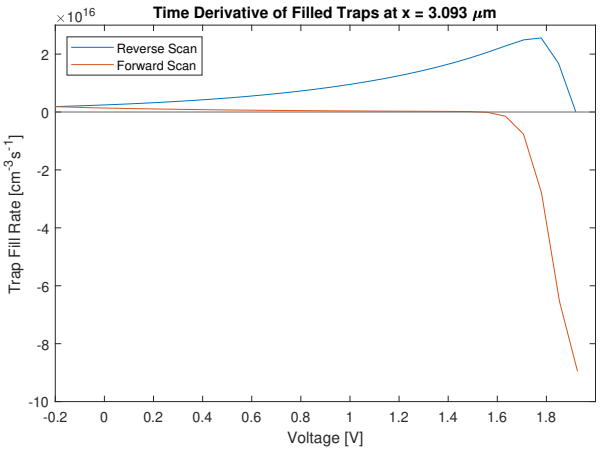

Figure 5.6: Trap fill rate at at x = 3.093 μm (or 12nm into the perovskite layer from the ETL interface) with positive values indicating filling and negative values emptying

In Figure 5.5 it can be seen that the quasi-Fermi level is slightly above the trap energy at the start of the reverse scan, which means a larger amount of the traps are expected to be filled, just like was expected based on Equation 2.7.

To show the speed of the trap filling and emptying, the fill rate was plotted in Figure 5.6. It can be seen that the fill rate increases for the first part of the reverse scan, until a peak, after which it slowly reaches zero during the forward scan. The probability distribution shown in Figure 2.3 shows that it is expected the traps start emptying again when the quasi-Fermi level is less than 0.1eV above the trap energy. This happens when the forward scan reaches 1.6V. When looking at Figure 5.6, it can indeed be seen that for this voltage the traps start emptying again.

When acceptor traps are filled, their charge changes from zero to negative. This is expected to affect the charge carrier extraction which then should result in a difference in the free carrier concentrations when comparing the forward and reverse scan. This can be seen in Figure 5.7.

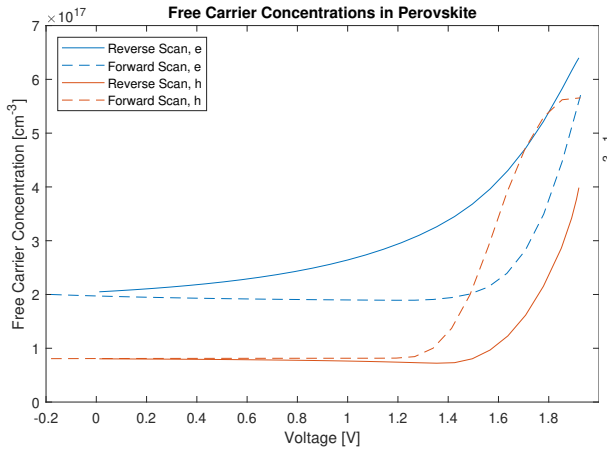

Figure 5.7: Free carrier concentrations in the perovskite layer during the forward and reverse scans

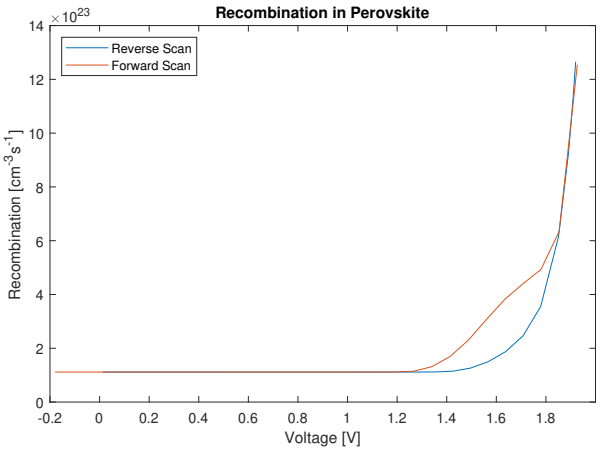

Figure 5.8: Total recombination in the perovskite layer for the reverse and forward scans

When looking at Figure 5.7, it shows that during the reverse scan, the minority charge carrier are holes, meaning the perovskite is slightly n-type. But during the forward scan, the minority charge carrier changes from holes to electrons, resulting in a p-type material until it becomes intrinsic at V_{OC}. This behaviour was found in other research, where they observed perovskite changing from seemingly n-type to p-type [109].

Then finally, because of the change in free charge carrier concentration between the forward scan and the reverse scan, the amount of recombination increases. As can be seen in Figure 5.8. And when flipping the shape of the recombination figure vertically, it can be seen that this shape resembles the hysteresis behaviour as depicted in Figure 4.1b.

5.1.2. HTL interface defects

The same way as the ETL interface defects were analysed, so will the HTL interface defects be looked at. The defect density at the interfaces is $2 \times 10^{18} cm^{-3}$ and the defects are donor-like. Furthermore, a defect energy of 0.18eV from the conduction band and a scan rate of $0.1V/s$ are used. These values resulted in the JV-curve in Fig 5.9. The quasi-Fermi level can be seen in Figure 5.10 for the voltages marked in the JV-curve. The trap energy is marked here with a line at $E_{Fn} - E_V = 1.5eV$.

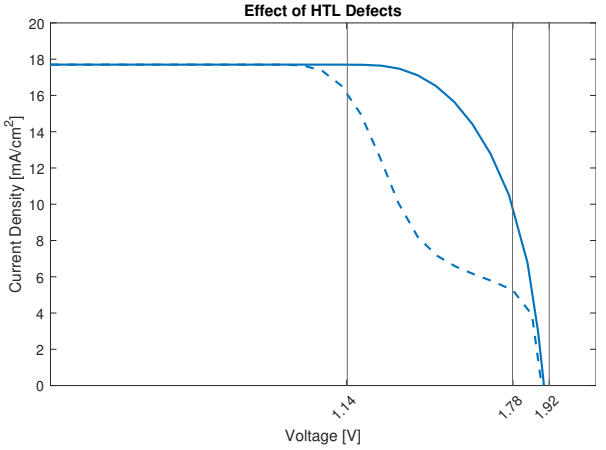

Figure 5.9: JV-curves for HTL defects with three voltage points marked for Fig. 5.10

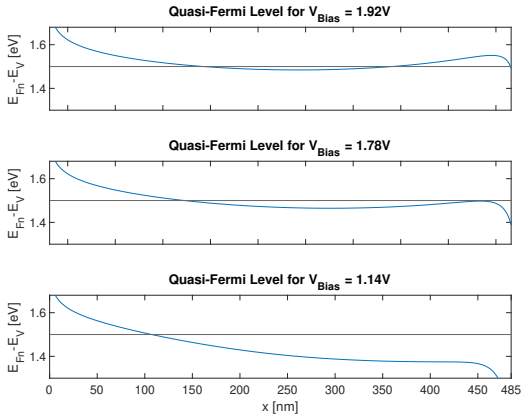

Figure 5.10: Quasi-Fermi level for the voltages marked in Fig. 5.1 during the reverse scan with the trap energy marked at 1.5eV

Just as for the ETL interface defects, it can be seen that for the HTL interface defects the quasi-Fermi level changes a lot near the interface as well. At first, it is above the trap energy for a certain portion, which indicates that more traps are empty than filled. As mentioned in Chapter 2, Sentaurus defines a filled donor-trap as a trap with positive charge. And later in the scan, the empty traps should fill since the quasi-Fermi level drops below their energies, making them positively charged. The change of filled trap concentration can be seen in Fig 5.11. The point at which the trap concentration changes most for this simulation is less than 3 nm from the interface (x=3.5638μ m when considering the whole cell). This can be expected since the quasi-Fermi level does not move to the middle of the band gap as significantly near the interface as for the ETL defects. On top of that, the concentration is higher near the interfaces because of the distribution. For this position the filled trap concentrations are again shown during the reverse and forward scan in Fig 5.12.

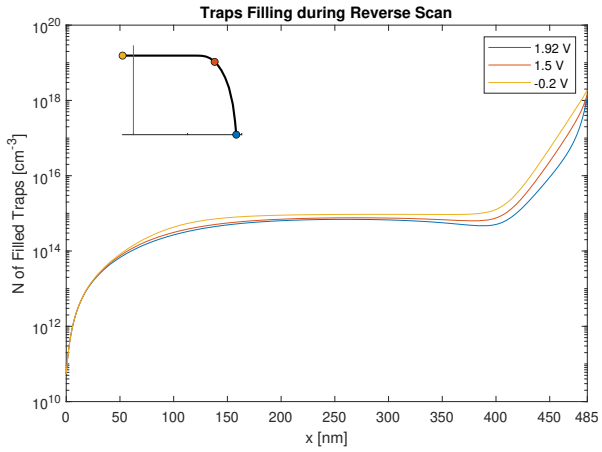

Figure 5.11: Concentration of filled traps in the perovskite layer for three voltages

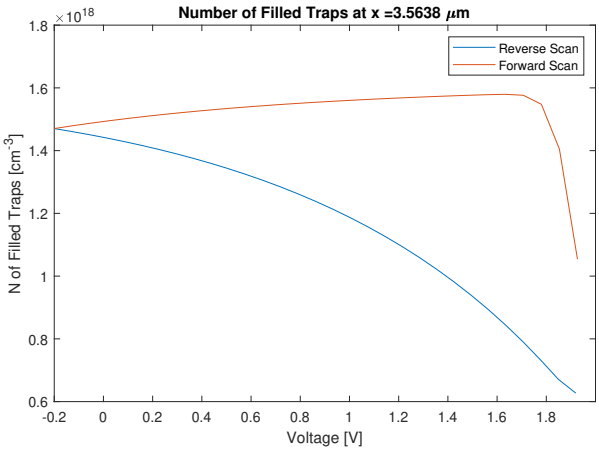

Figure 5.12: Concentration of filled traps at x= 3.5638 μm (or 3nm into the perovskite layer from the HTL interface)

The filled trap concentration figure shows the same trend as for the ETL interface defects, only for higher values. This is because the analysis point is closer to the interface. Indicating that less than half of the traps are expected to be filled. So based on Eq. 2.8, the quasi-Fermi level should be just above the trap energy at this point. Which is verified in Figure 5.13. During the simulation, traps keep filling until the quasi-Fermi energy reaches a value of 0.1eV below the trap energy during the forward scan, after which the traps start emptying again. It can be seen this happens around 1.6V in Figure 5.14.

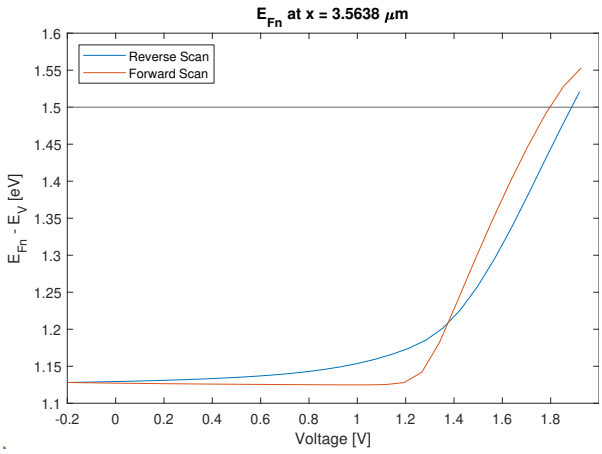

Figure 5.13: Quasi-Fermi level at x= 3.5638 μm (or 3nm into the perovskite layer from the HTL interface)

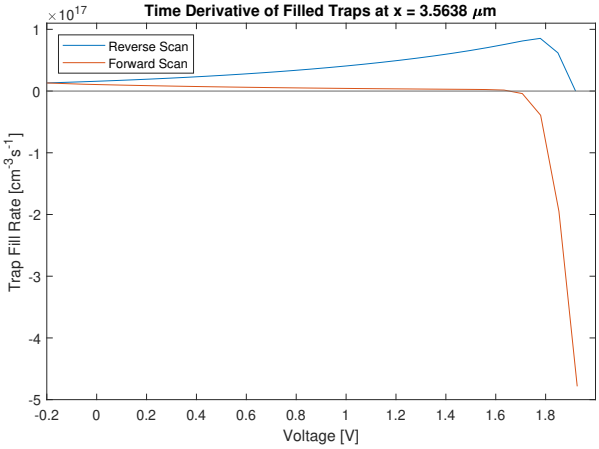

Figure 5.14: Trap fill rate at x= 3.5638 μm (or 3nm into the perovskite layer from the HTL interface) with positive values indicating filling and negative values emptying

The donor traps have a positive charge when filled. This means that when the traps are filled near the HTL layer, holes are repelled by the positive charges. Resulting in less charge extraction. This then has an effect on the free carrier concentrations. For the HTL interface defects, the minority carriers in the perovskite are holes, with the electron concentrations significantly higher, making it an n-type material. It can be seen that the traps have influenced the hole concentration in the perovskite layer when looking at Figure 5.15.

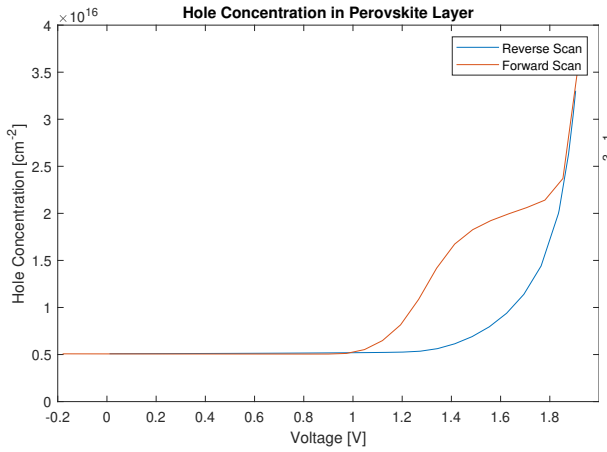

Figure 5.15: Free carrier concentrations in the perovskite layer during the forward and reverse scan

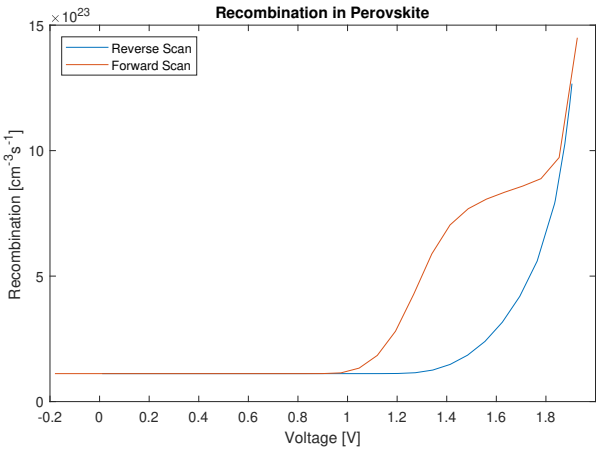

Figure 5.16: Total recombination in the perovskite layer for the reverse and forward scans

The difference in hole concentration when comparing the reverse and forward scans result in the total recombination in the layer deviating as well. As can be seen in Figure 5.16. This figure, when flipped vertically, fits the shape of the hysteresis behaviour as depicted in Figure 4.1c, just as for the ETL interface defects.

5.2. Effect of scan rate

To explain the shape of Fig. 4.3, the number of filled traps during the scan and their fill rates are looked at. When looking at the figure, it can be seen that for a slower scan rate of 0.01 V/s, the HI is low. Then for a scan rate of 0.1 V/s it reaches a maximum, after which it falls back to a lower value at 1 V/s.

When looking at the JV-curves for these values, it can be seen that for the 0.01 V/s scans, the reverse and forward scans both perform worse than for no-defects behaviour. For the 0.1 V/s simulation, the forward scan is affected most and the reverse only slightly. Lastly for 1 V/s, both scans are hardly affected by the defects. This behaviour can be explained by looking at Figure 5.17. The figure shows the trap concentrations during the reverse (blue) and forward (red) scans for the different scan rates.

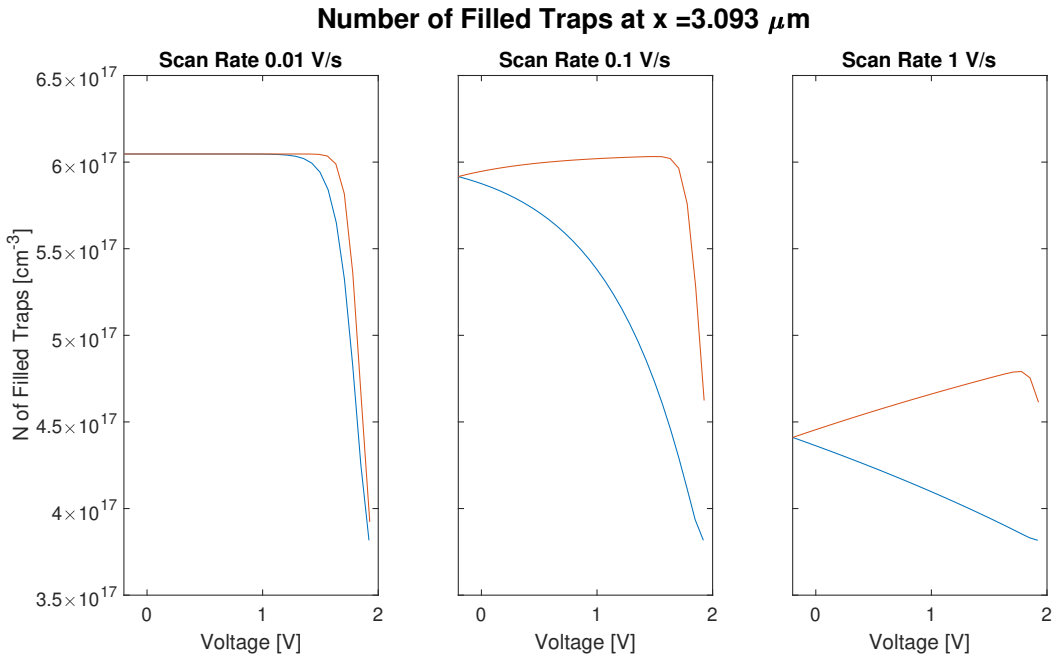

Figure 5.17: Filled trap concentrations at x = 3.093 μm for different scan rates with reverse scan in blue and forward scan in red

In the trap concentration figures, it becomes evident why the hysteresis index peaks for 0.1 V/s. For this scan rate, the traps are fully filled, just before they start emptying again because the quasi-Fermi level is close enough to the trap energy. This results in the biggest difference between the forward and reverse scans. For the 0.01 V/s simulation, the traps are already filled just after initialising the reverse scan, resulting in worse performance for both scans. The fast scan rate of 1 V/s means that the traps do not have time to fill, hardly affecting the reverse and forward scans as a result. This behaviour is made more apparent when looking at the fill rates for the voltage sweeps in Figure 5.18. In these plots, the fill rates during the reverse (blue) and forward (red) scans for the different scan rates can be seen.

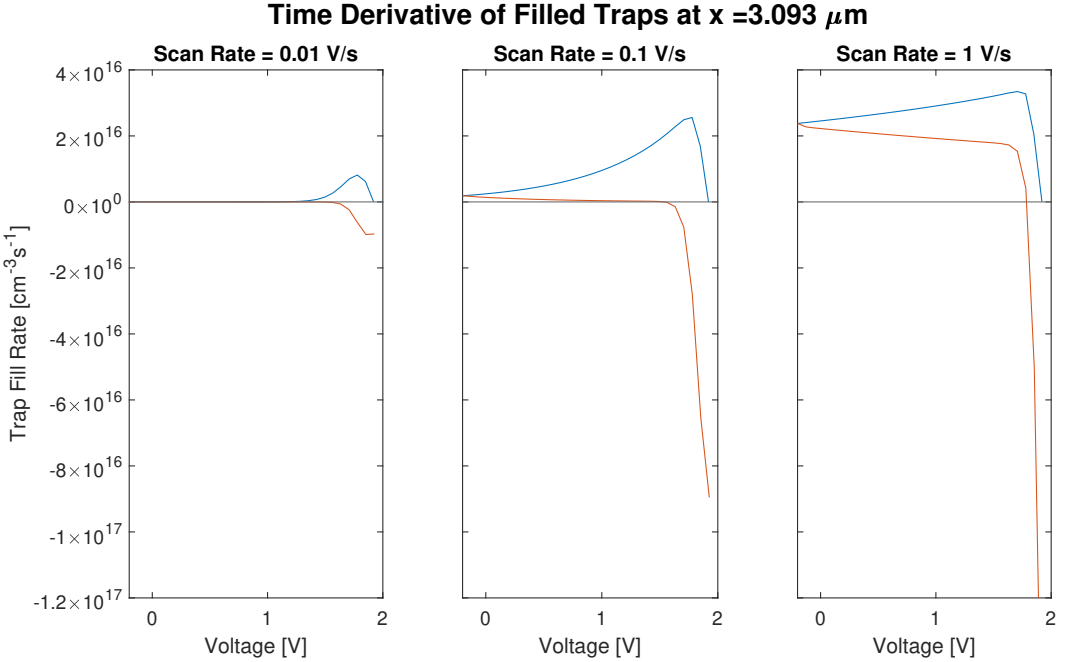

Figure 5.18: Trap fill rates at x = 3.093 μm for different scan rates with reverse scan in blue and forward scan in red

The fill rate figure shows the traps stop filling very early on in the reverse scan for the 0.01 V/s scan, indicated by a fill rate of zero. The 0.1 V/s case reaches the zero point just before the forward scan hits 1.6V, the point where the traps would start emptying again. Lastly it becomes evident most traps are still not filled when looking at the 1 V/s simulation.

5.3. Effect of defect energy

As can be seen in Figure 4.10, the hysteresis index is affected by the trap energy. Figure 5.19 shows the trap concentrations during the reverse and forward scans for different trap energy levels. These simulations were all done for a defect concentration of $2 \times 10^{18} cm^{-3}$ near the ETL, and a scan rate of 0.1 V/s. The trap concentration shows similar behaviour as for the simulations with different scan rates in Section 5.2, but for different reasons.

When looking at Figure 5.19, it can be seen that, just like for the 0.01 V/s scan rate in Figure 5.17, the traps fill early on in the reverse scan. The traps with a trap energy of 0.24eV are the same as the other ETL defects modelled before, so the traps are completely filled just before they start emptying again. For the 0.26eV traps however, they do not reach this point of all traps being filled. It should also be noted that a higher trap energy means the reverse scan starts with a lower amount of filled traps.

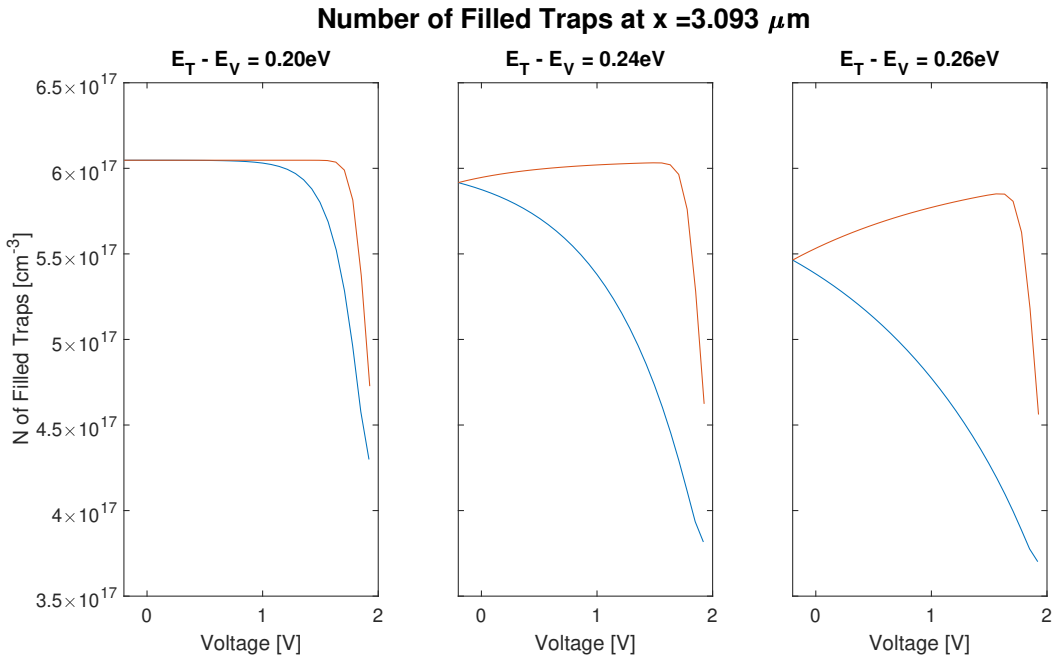

Figure 5.19: Filled trap concentrations at x = 3.093 μm for different trap energies with reverse scan in blue and forward scan in red

To more prominently show at what point the traps start emptying, the fill rates are plotted out again in Figure 5.20. It can be noted that for lower trap energies, the filling is quicker.

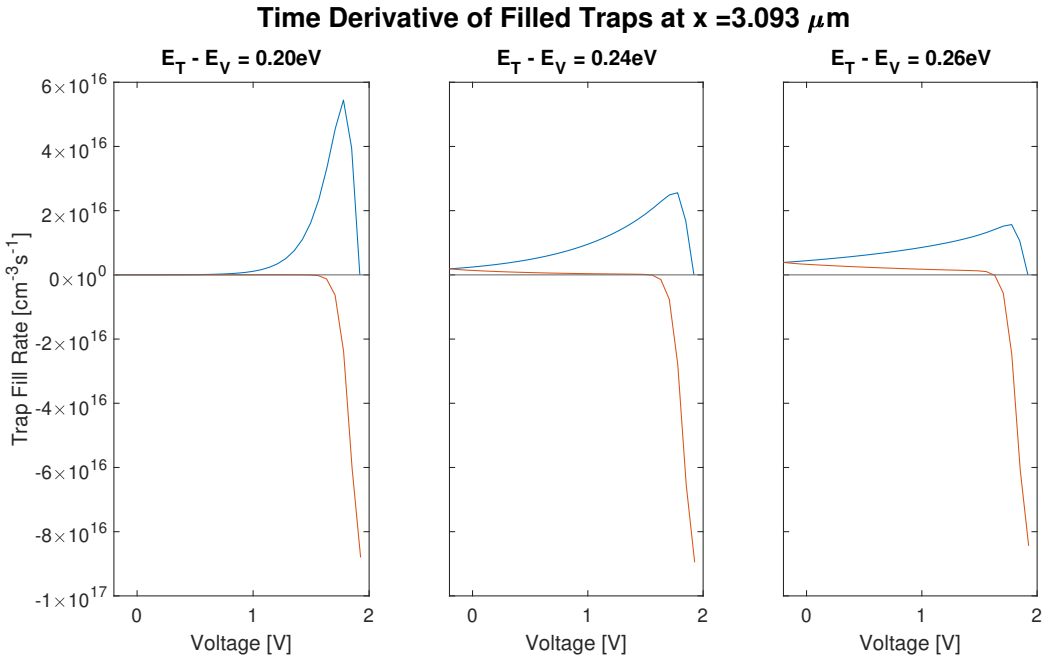

Figure 5.20: Trap fill rates at x = 3.093 μm for different trap energies with reverse scan in blue and forward scan in red

The quicker filling and difference in the hysteresis behaviour can be explained when looking at Figure 5.21. The figure shows the quasi-Fermi levels during the reverse and forward scans for different trap energies. The trap level energies have been marked with a horizontal line.

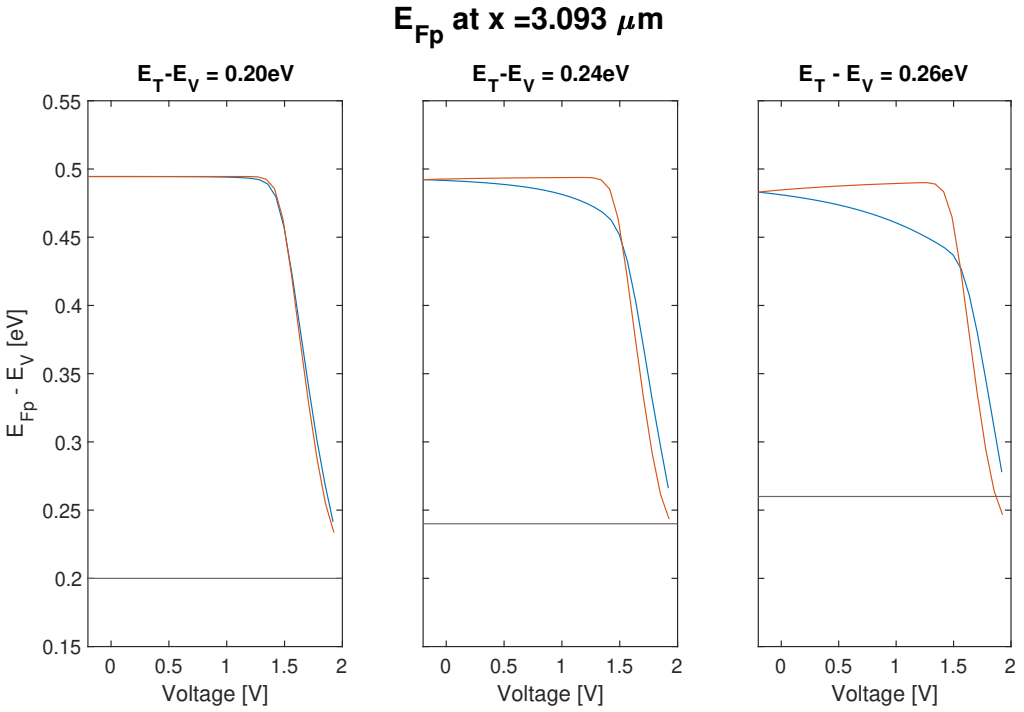

Figure 5.21: Quasi-Fermi energies at x = 3.093 μm for different trap energies with reverse scan in blue and forward scan in red and the trap energy marked with a horizontal line

As can be seen for the 0.20eV traps, the quasi-Fermi level is a lot higher compared to the trap energy than for the other traps. This results in them filling more quickly and reaching full capacity early on,

which results in the behaviour of the cell being similar for reverse and forward scan. The traps with an energy of 0.24eV have already been analysed with Figure 5.5. The quasi-Fermi level for the 0.26eV traps starts close to the trap energy, resulting a less traps filled at the start of the reverse scan.

5.4. Effect of defect density

The results chapter showed that the amount of defects influenced the severity of the hysteresis behaviour immensely. Although this is as expected, it is good to look at the fundamentals as to why this is. First the ETL defects are analysed. Figure 5.23 shows the same trap concentration plot as before, to compare it to Figure 5.22, with a trap concentration of $1 \times 10^{18} cm^{-3}$ near the interface.

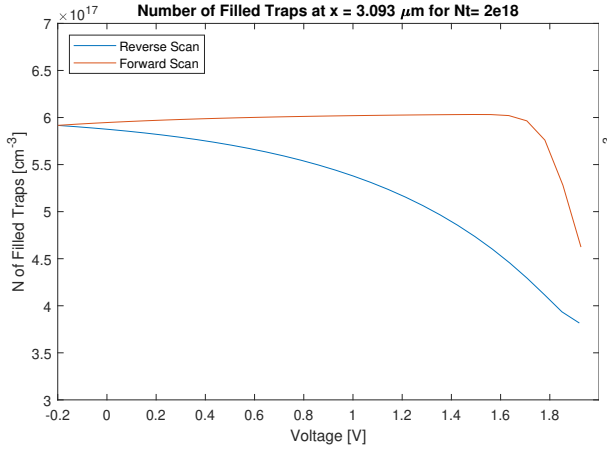

Figure 5.22: Filled trap concentrations at x = 3.093 μm for a defect density of 2×10^{18} near the ETL interface

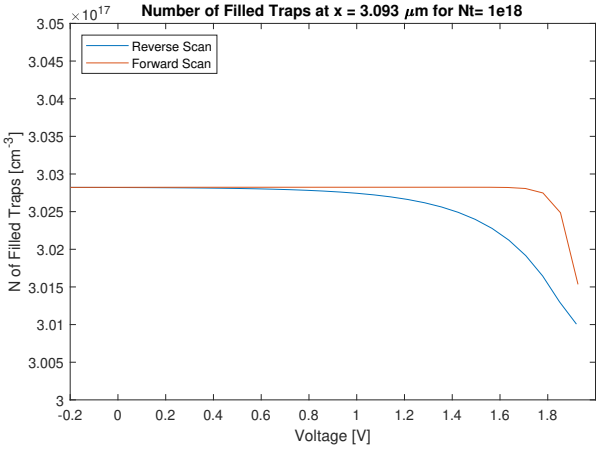

Figure 5.23: Filled trap concentrations at x = 3.093 μm for a defect density of 1×10^{18} near the ETL interface

When looking at this figure, it becomes evident only an extremely small portion of the traps is still filling at the start of the reverse scan. At the analysis point, the total trap concentration is about 3.03×10^{17}, which means they are almost all completely filled at the beginning of the reverse scan. Figure 5.24 shows why. This figure compares the quasi-Fermi levels throughout the simulation for the two different defect densities.

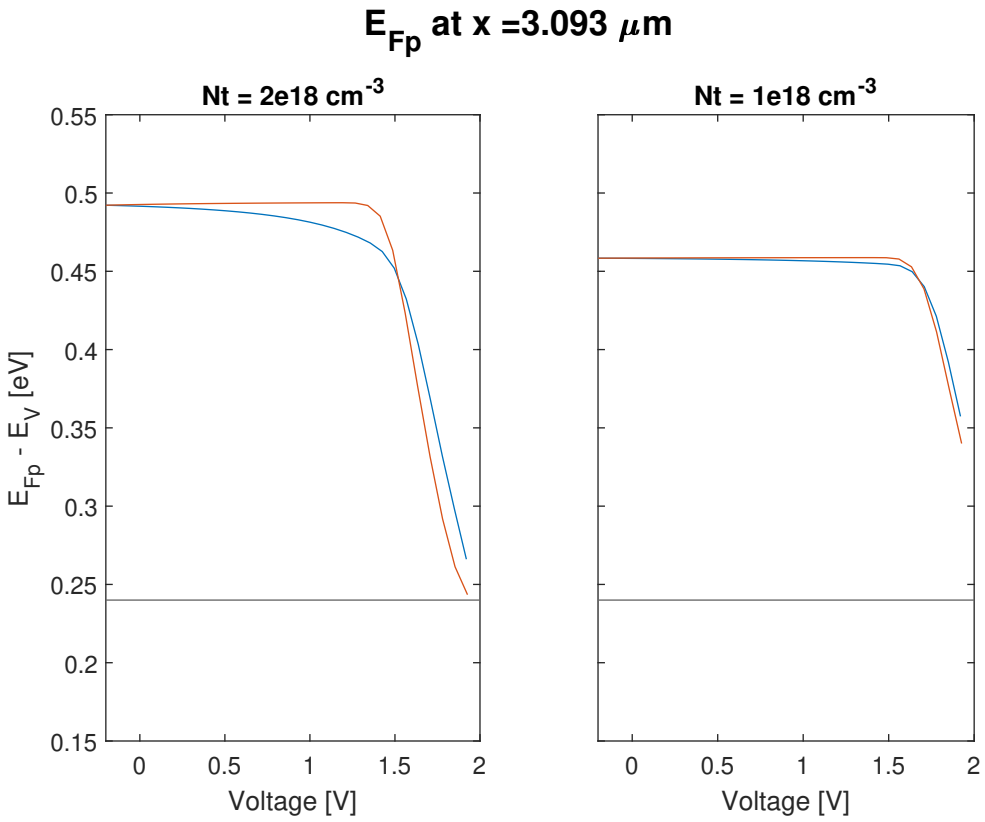

Figure 5.24: Quasi-Fermi level at x = 3.093 μm for different defect densities near the ETL interface with reverse scan in blue and forward scan in red

First of all, it becomes evident the quasi-Fermi levels of the reverse and forward scan for the lower density are almost similar, resulting in no hysteresis. On top of that, the quasi-Fermi level for the lower defect density is already more than 0.1eV above the trap energy when the simulation starts, indicating that almost all the traps should be filled. The quasi-Fermi energy barely reaches this energy difference at the end of the forward scan resulting in a very small amount of traps emptying. This indicates that the trap density influences how low the quasi-Fermi level can go, resulting in the traps being empty or not. The same trend holds for the HTL defects.

5.5. Effect of architecture

It became obvious from the results that the SJ and tandem cells showed differences in how severe the hysteresis was. By normalizing the JV-curves in Sec 4.7, it was explained that this is probably because of the current-limiting bottom cell. This resulted in the higher hysteresis index values computed. In this section the reasons for this will be investigated. To be able to compare the tandem and SJ cell fairly, the voltage has been normalized.

5.5.1. ETL defects

For the ETL interface defects, both the tandem and SJ trap filling and quasi-Fermi levels follow the trends shown in the previous sections. The biggest difference is shown when looking at Figures 5.25 and 5.26. These figures show the free carrier concentrations in the entirety of the perovskite layer. When the bottom cell is current-limiting, the top cell creates more charge carriers than can be passed to the bottom cell, resulting in a higher free carrier concentration since they can not be moved away.

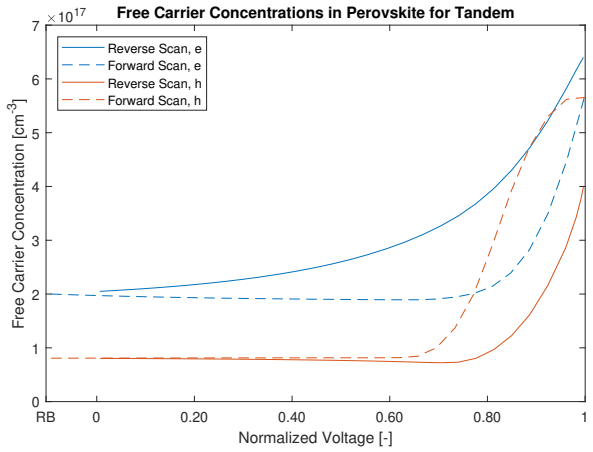

Figure 5.25: Free carrier concentrations in the perovskite layer for a tandem architecture

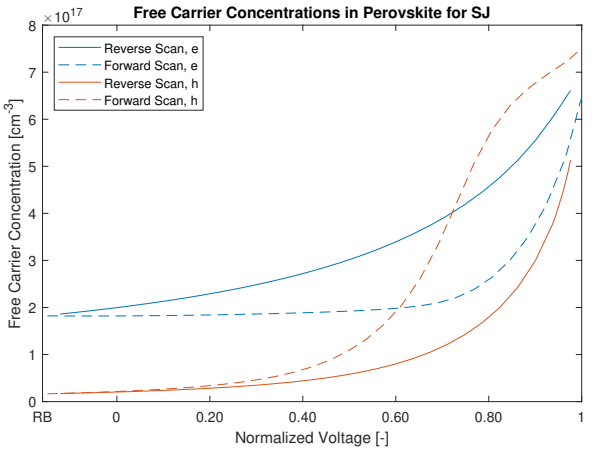

Figure 5.26: Free carrier concentrations in the perovskite layer for a SJ architecture

The current-limiting becomes apparent when looking at the figures. When the normalized voltage goes down during the reverse scan for the tandem, at around 80 percent, the hole density reaches a threshold. The reason for this is that the bottom cell can not extract more charge carriers since it does not generate enough itself. This is not the case for the SJ cell. The increased hole density at the end of the forward scan is likely a consequence of the architecture. It seems the hole extraction is better in the tandem cell, likely because it has the TRJ, which increases the amount of good recombination. This should make the hole extraction from the HTL, and as a consequence from the perovskite, better.

The free carrier concentrations affect the amount of recombination. This can be seen in Figures 5.27 and 5.28. Because the free carrier density has a threshold it can not go under for the tandem, the recombination stays higher as well. But this behaviour is for both reverse and forward scan. The SJ does not have this limit, so has less recombination, but the reverse scan performs better than the forward scan, resulting in more hysteresis. It can also be seen that the the forward scan performs slightly worse for the SJ cell for the region where the tandem is not current-limited. This is a result of the amount of free charge carriers being slightly higher.

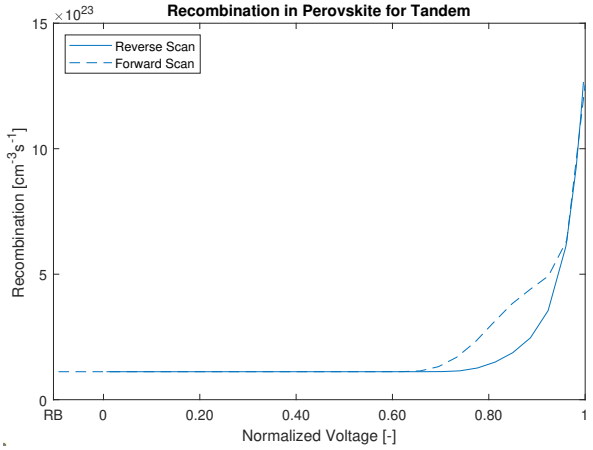

Figure 5.27: Recombination in the perovskite layer for a tandem architecture

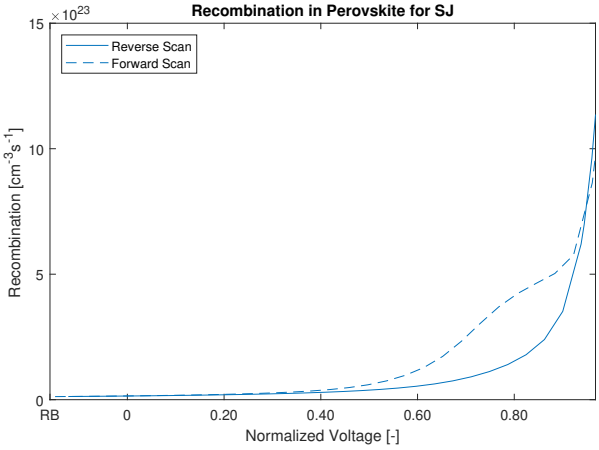

Figure 5.28: Recombination in the perovskite layer for a SJ architecture

5.5.2. HTL defects

For the HTL interface defects, the number of traps and quasi-Fermi level differ a lot when compared. The filled trap concentrations for the HTL defects can be seen in Figures 5.29 and 5.30. The most notable difference between the figures is that the filled trap concentration during the reverse scan is a lot higher for the SJ than for the tandem. On top of that, the SJ traps seem to fill and empty slower. The slower

filling and emptying can be explained by the fact that even though the scan rate is the same, the lower open circuit voltage of the SJ means the entire scan takes less time. This gives the traps less time to fill and empty, and because of the normalized voltage, this seems like they behave slower.

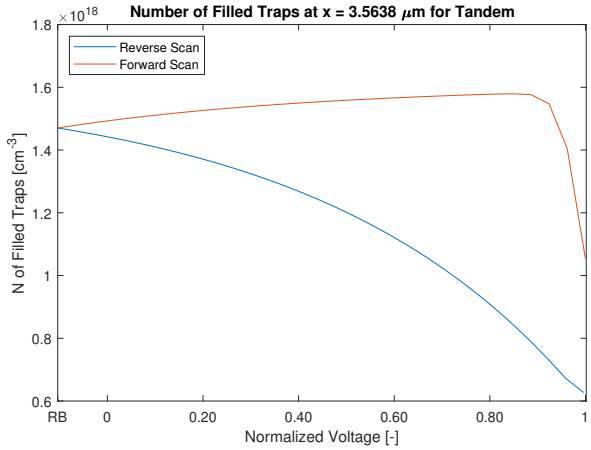

Figure 5.29: Filled trap concentration at x = 3.5638 μm for a tandem architecture

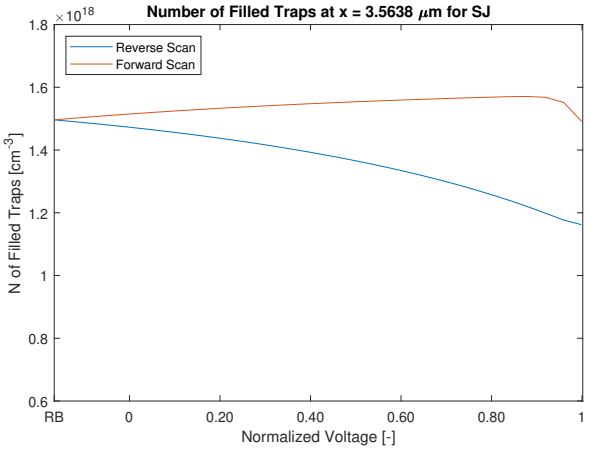

Figure 5.30: Filled trap concentration at x = 3.5638 μm for a SJ architecture

The higher filled trap concentration during the reverse scan can be explained when comparing Figures 5.31 and 5.32. It is clear the quasi-Fermi level for the SJ starts at a lower energy, below the trap energy, for the reverse scan. This means it is expected more traps are filled, just like can be seen in the filled trap concentration figure.

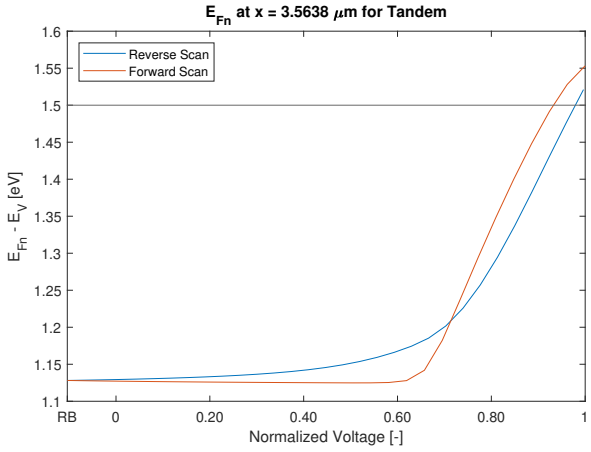

Figure 5.31: Quasi-Fermi levels at x = 3.5638 μm for a tandem architecture

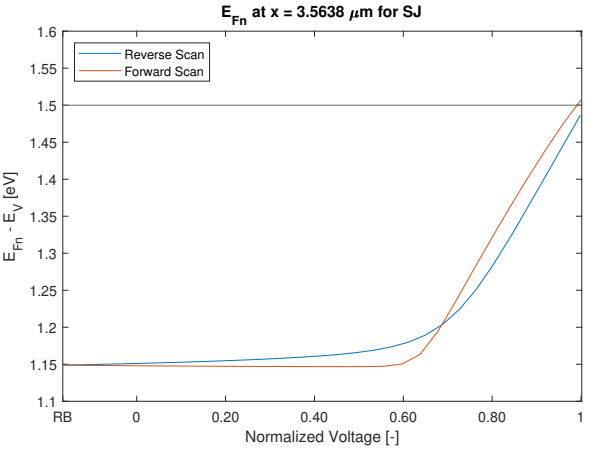

Figure 5.32: Quasi-Fermi levels at x = 3.5638 μm for a SJ architecture

The effect of the filled traps on the free carrier concentrations can be seen in Figures 5.33 and 5.34. The same current-limiting behaviour as for the ETL defects can be found. Other than that, the amount of free holes in both reverse and forward scans is slightly higher for the SJ than for the tandem. This is a consequence of the filled trap concentration being higher for both scans.

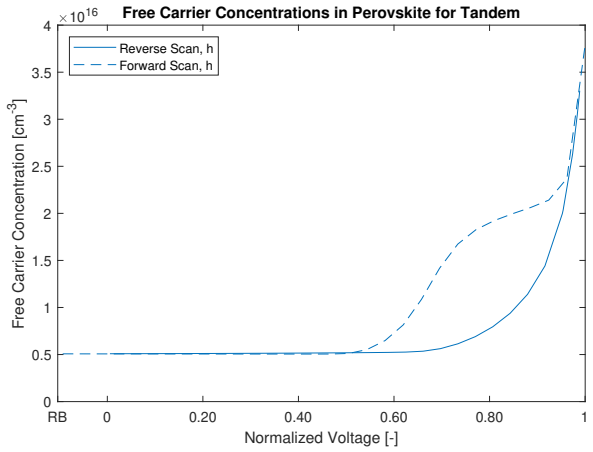

Figure 5.33: Free hole concentrations in the perovskite layer for a tandem architecture

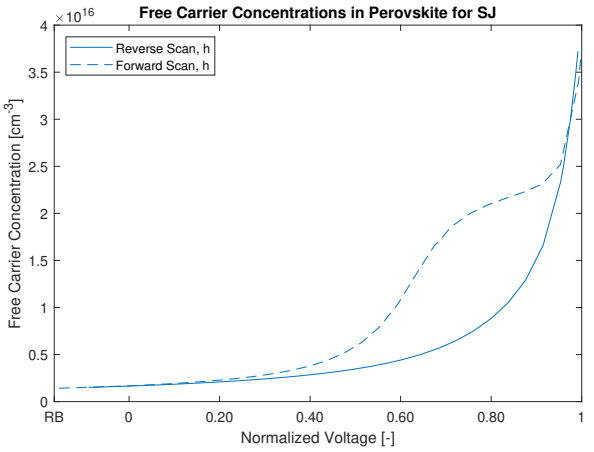

Figure 5.34: Free hole concentrations in the perovskite layer for a SJ architecture

The difference in the free hole concentrations results in a similar deviation in the recombination values as can be seen in Figures 5.35 and 5.36. The small differences shown in Figure 4.15 for the forward scan can be explained with the quasi-Fermi level, which indicates a small increase in hysteresis. However, the larger increase in hysteresis as found in the results is mainly caused by the current-limiting.

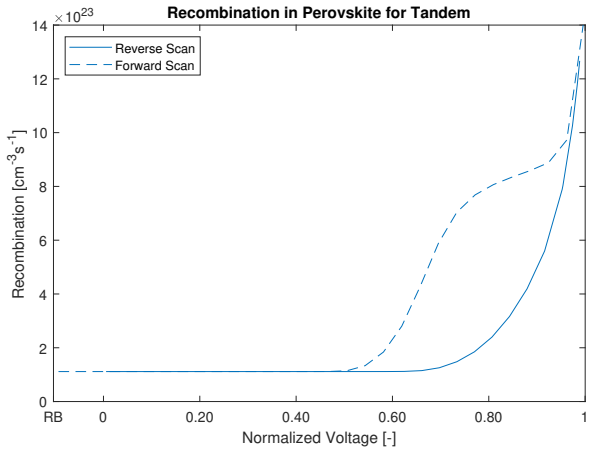

Figure 5.35: Recombination in the perovskite layer for a tandem architecture

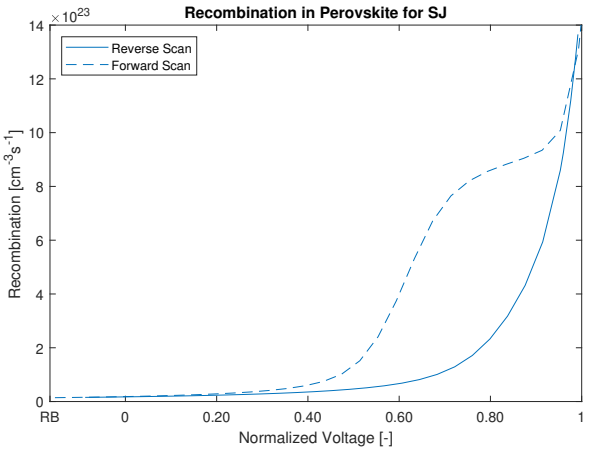

Figure 5.36: Recombination in the perovskite layer for a SJ architecture

5.6. Traps in silicon layers

The focus of this research is on the perovskite layer within the tandem. However, the defects in the c-Si layer seem to have a significant effect on the hysteresis index. The hysteresis index starts to increase rapidly for scan rates higher than 10 V/s as can be seen in Figure 4.3. The range of the simulations does not reveal at what value the peak is however. This behaviour can not be explained by looking at the defects in the perovskite, so it is expected the explanation lies in the bottom cell. Herman et al. [106] found significant hysteresis in a crystalline silicon cell for scan rates of 130 V/s and higher. This seems to be in line with the results gathered in Chapter 4.

5.7. Ion migration

As stated before, ion migration is the most common explanation for the hysteresis behaviour [110, 111, 112, 113]. So far, most research uses this mechanism to simulate and research the hysteresis behaviour in perovskite materials. Although hysteresis can be modelled this way and there is evidence ions migrate throughout the perovskite, it can not explain the complete picture of hysteresis in these materials. The main problem with this approach is found in the more recent perovskite solar cells. Using passivation

and defect engineering, research has reported there to be either no or low amounts of hysteresis [114]. These solutions are difficult to explain using ion migration, but fit better when considering hysteresis caused by defects.

This does not mean, however, that ion migration is not displayed in perovskite layers, rather that ion migration and defects are likely both responsible for hysteresis. The migrating ions can be seen as defects if they have energy levels within the perovskite bandgap. One of the ions to be expected to migrate throughout perovskite materials is iodine, I^-. This anion has an energy level of around 0.18eV above E_V [115], falling within the range to induce hysteresis as found in Section 4.6. Iodine anions can be classified as interstitial defects as displayed in Figure 2.4.

5.8. Conclusion

Using the underlying theory of Chapter 2, the effect of defects on the hysteresis behaviour was shown. It was explained that the changing of the quasi-Fermi levels during the voltage sweeps resulted in the traps filling and emptying. This then, would change the charge of the traps which influenced carrier recombination. This ultimately induced the hysteresis behaviour. Using this theory as a stepping stone, the difference between tandem and single-junction cell hysteresis behaviour was explained. Ion migration was discussed as well, concluding that it can not explain the hysteresis behaviour on its own, but that ion migration and defects are expected to work complementary.

6

Conclusion and recommendations

In this report, it was shown the hysteresis behaviour can be modelled using defects. First, a method was developed to simulate hysteresis behaviour in a perovskite / c-Si tandem cell using defects. This was done based on previous work and adapted to a more sophisticated tandem cell. Using this method, it was possible to simulate the tandem cell, and to compare it to a single-junction cell.

Based on literature, certain variables were expected to influence the hysteresis mechanism. These expectations were investigated to explain the hysteresis behaviour as a result of defects. The effect of defect density, capture cross-section energy levels, and Urbach tail states was shown. The results showed that for both the tandem and the single-junction device, significant hysteresis was present for

- defect densities higher than 2×10^{18} for ETL interface defects and 1×10^{18} for HTL interface defects
- the right combination of capture cross section and scan rate
- ETL defect energies of 0.24eV for the tandem and 0.23eV for the SJ, and HTL defects energies of 1.5eV for the tandem and 1.51eV for the SJ (when compared to the valence band)

With the ETL interface defects being acceptor-like and HTL interface defects being donor-like. Although the simulation software is able to model every defect energy level, in reality not all of these levels can exist. The resulting ETL defect energies can be coupled to iodine, but the energy range for the HTL defects have no realistic causes in physical perovskite cells. The most important result was that the tandem and single-junction behaviours were similar but not equal, with their biggest difference finding its cause in current-limiting.

In short, hysteresis behaviour was simulated in a perovskite / c-Si tandem cell using defects. Using the theory, the results of the simulations were explained, and with that, the difference between the hysteresis behaviour of the tandem and single-junction cells was found. By taking a deeper look into the mechanisms in the perovskite layer, the explanation for the hysteresis behaviour as a result of defects was uncovered.

6.1. Recommendations

To reach an even more realistic model, a couple of steps can be taken. The biggest improvements would be found in including an ion migration model and in calibrating the model variables with measurements. As explained earlier, ion migration likely functions complementary to the defect model, it would be interesting to research this hypothesis. Furthermore, the amount of measurements available is still very low, especially for this exact cell type. The modelling and fabrication of the same perovskite tandem cell could help in calibrating the hysteresis behaviour and determining how realistic the found results are. Some smaller possible improvements can be found in the defect distribution and capture cross-sections. The defect distribution shape approaches measured data, but is not completely realistic, it would be good to investigate to what extend this affects the hysteresis. The capture cross-sections for holes and electrons were kept similar for this report, based on previous research saying this resulted in more hysteresis. Since they influence the speed of the capture and release of charge, having different values is still expected to change the hysteresis behaviour.

Lastly, to even further investigate what happens inside the perovskite layer during hysteresis, the tandem cell structure could be changed. It would be interesting to see if there is still a big difference in hysteresis between tandem and SJ behaviour if the tandem is not current-limited by the c-Si layer. To investigate this, the layer thicknesses need to be reevaluated to ensure the generation is equal or in favour of the c-Si layer.

References

[1] Arno Smets et al. *Solar Energy: The physics and engineering of photovoltaic conversion, technologies and systems*. Cambridge, UNITED KINGDOM: UIT Cambridge Ltd., 2016.

[2] A. Einstein. "Über einen die Erzeugung und Verwandlung des Lichtes betreffenden heuristischen Gesichtspunkt". en. In: *Annalen der Physik* 322.6 (1905), pp. 132–148.

[3] Fraunhofer. *Photovoltaics Report*. en.

[4] PCC Group. *Elements in the Earth's crust*. en.

[5] William Shockley and Hans J. Queisser. "Detailed Balance Limit of Efficiency of p-n Junction Solar Cells". In: *Journal of Applied Physics* 32 (Mar. 1961), pp. 510–519.

[6] NREL. *Best Research-Cell Efficiency Chart*. en.

[7] F. Meillaud et al. "Efficiency limits for single-junction and tandem solar cells". In: *Solar Energy Materials and Solar Cells*. 14th International Photovoltaic Science and Engineering Conference 90.18 (Nov. 2006), pp. 2952–2959.

[8] WEBMINERAL. *Perovskite Mineral Data*.

[9] Martin A. Green, Anita Ho-Baillie, and Henry J. Snaith. "The emergence of perovskite solar cells". en. In: *Nature Photonics* 8.7 (July 2014), pp. 506–514.

[10] Christian Wehrenfennig et al. "High Charge Carrier Mobilities and Lifetimes in Organolead Trihalide Perovskites". In: *Advanced Materials* 26.10 (2014), pp. 1584–1589.

[11] Samuel D. Stranks et al. "Electron-Hole Diffusion Lengths Exceeding 1 Micrometer in an Organometal Trihalide Perovskite Absorber". In: *Science* 342.6156 (Oct. 2013), pp. 341–344.

[12] Carlito S. Jr. Ponseca et al. "Organometal Halide Perovskite Solar Cell Materials Rationalized: Ultrafast Charge Generation, High and Microsecond-Long Balanced Mobilities, and Slow Recombination". In: *Journal of the American Chemical Society* 136.14 (Apr. 2014), pp. 5189–5192.

[13] Guichuan Xing et al. "Long-Range Balanced Electron- and Hole-Transport Lengths in Organic-Inorganic CH3NH3PbI3". In: *Science* 342.6156 (Oct. 2013), pp. 344–347.

[14] Jun Hong Noh et al. "Chemical Management for Colorful, Efficient, and Stable Inorganic–Organic Hybrid Nanostructured Solar Cells". In: *Nano Letters* 13.4 (Apr. 2013), pp. 1764–1769.

[15] Moritz H. Futscher and Bruno Ehrler. "Efficiency Limit of Perovskite/Si Tandem Solar Cells". In: *ACS Energy Letters* 1.4 (Oct. 2016), pp. 863–868.

[16] Leiping Duan et al. "Stability challenges for the commercialization of perovskite–silicon tandem solar cells". en. In: *Nature Reviews Materials* 8.4 (Apr. 2023), pp. 261–281.

[17] Martin A. Green. "Ag requirements for silicon wafer-based solar cells". en. In: *Progress in Photovoltaics: Research and Applications* 19.8 (2011), pp. 911–916.

[18] Michele De Bastiani et al. "Toward Stable Monolithic Perovskite/Silicon Tandem Photovoltaics: A Six-Month Outdoor Performance Study in a Hot and Humid Climate". In: *ACS Energy Letters* 6.8 (Aug. 2021), pp. 2944–2951.

[19] Rui Chen et al. "Rear Electrode Materials for Perovskite Solar Cells". en. In: *Advanced Functional Materials* 32.26 (2022), p. 2200651.

[20] Erkan Aydin et al. "Enhanced optoelectronic coupling for perovskite/silicon tandem solar cells". en. In: *Nature* 623.7988 (Nov. 2023), pp. 732–738.

[21] X. Tong et al. "High performance perovskite solar cells". English. In: *Advanced Science* 3.5 (2015).

[22] A. Gheno et al. "pi-Conjugated materials as the hole-transporting layer in perovskite solar cells". English. In: *Metals* 6.1 (2016).

[23] S. Ameen et al. “Perovskite Solar Cells: Influence of Hole Transporting Materials on Power Conversion Efficiency”. English. In: *ChemSusChem* 9.1 (2016), pp. 10–27.

[24] Z. Yu and L. Sun. “Recent Progress on Hole-Transporting Materials for Emerging Organometal Halide Perovskite Solar Cells”. English. In: *Advanced Energy Materials* 5.12 (2015).

[25] W.-Y. Chen et al. “Low-cost solution-processed copper iodide as an alternative to PEDOT:PSS hole transport layer for efficient and stable inverted planar heterojunction perovskite solar cells”. English. In: *Journal of Materials Chemistry A* 3.38 (2015), pp. 19353–19359.

[26] Y. Wang et al. “Towards printed perovskite solar cells with cuprous oxide hole transporting layers: A theoretical design”. English. In: *Semiconductor Science and Technology* 30.5 (2015).

[27] X. Yin et al. “High efficiency hysteresis-less inverted planar heterojunction perovskite solar cells with a solution-derived NiOx hole contact layer”. English. In: *Journal of Materials Chemistry A* 3.48 (2015), pp. 24495–24503.

[28] A.S. Subbiah et al. “Inorganic hole conducting layers for perovskite-based solar cells”. English. In: *Journal of Physical Chemistry Letters* 5.10 (2014), pp. 1748–1753.

[29] T. Zhang et al. “Controllable Sequential Deposition of Planar CH3NH3PbI3 Perovskite Films via Adjustable Volume Expansion”. English. In: *Nano Letters* 15.6 (2015), pp. 3959–3963.

[30] Y. Guo et al. “Enhancement in the efficiency of an organic-inorganic hybrid solar cell with a doped P3HT hole-transporting layer on a void-free perovskite active layer”. English. In: *Journal of Materials Chemistry A* 2.34 (2014), pp. 13827–13830.

[31] Nevena Marinova, Silvia Valero, and Juan Luis Delgado. “Organic and perovskite solar cells: Working principles, materials and interfaces”. In: *Journal of Colloid and Interface Science* 488 (Feb. 2017), pp. 373–389.

[32] Amran Al-Ashouri et al. “Monolithic perovskite/silicon tandem solar cell with >29% efficiency by enhanced hole extraction”. In: *Science* 370.6522 (Dec. 2020), pp. 1300–1309.

[33] Silvia Mariotti et al. “Interface engineering for high-performance, triple-halide perovskite-silicon tandem solar cells”. eng. In: *Science (New York, N.Y.)* 381.6653 (July 2023), pp. 63–69.

[34] Silvia Colella et al. “MAPbI3-xClx Mixed Halide Perovskite for Hybrid Solar Cells: The Role of Chloride as Dopant on the Transport and Structural Properties”. In: *Chemistry of Materials* 25.22 (Nov. 2013), pp. 4613–4618.

[35] Maria Azhar et al. “Damping the phase segregation in mixed halide perovskites: Influence of X-site anion”. In: *Materials Chemistry and Physics* 287 (Aug. 2022), p. 126335.

[36] Khalid Mahmood, Saad Sarwar, and Muhammad Taqi Mehran. “Current status of electron transport layers in perovskite solar cells: materials and properties”. en. In: *RSC Advances* 7.28 (2017), pp. 17044–17062.

[37] Xin-Feng Diao et al. “Study on the Property of Electron-Transport Layer in the Doped Formamidinium Lead Iodide Perovskite Based on DFT”. In: *ACS Omega* 4.22 (Nov. 2019), pp. 20024–20035.

[38] F. A. Rubinelli, J. K. Rath, and R. E. I. Schropp. “Microcrystalline *n-i-p* tunnel junction in a-Si:H/a-Si:H tandem cells”. en. In: *Journal of Applied Physics* 89.7 (Apr. 2001), pp. 4010–4018.

[39] Leo Esaki. *Long Journey into Tunneling*. en.

[40] Guangyi Wang et al. “Understanding and design of efficient carrier-selective contacts for solar cells”. en. In: *AIP Advances* 11.11 (Nov. 2021), pp. 115026–9.

[41] Martin A. Green. “The Passivated Emitter and Rear Cell (PERC): From conception to mass production”. In: *Solar Energy Materials and Solar Cells* 143 (Dec. 2015), pp. 190–197.

[42] Gerard Masmitjà et al. “V2Ox-based hole-selective contacts for c-Si interdigitated back-contacted solar cells”. en. In: *Journal of Materials Chemistry A* 5.19 (May 2017), pp. 9182–9189.

[43] Xinbo Yang et al. “Tantalum Nitride Electron-Selective Contact for Crystalline Silicon Solar Cells”. en. In: *Advanced Energy Materials* 8.20 (2018), p. 1800608.

[44] James Bullock et al. “Lithium Fluoride Based Electron Contacts for High Efficiency n-Type Crystalline Silicon Solar Cells”. en. In: *Advanced Energy Materials* 6.14 (2016), p. 1600241.

[45] Jian He et al. “Stable Electron-Selective Contacts for Crystalline Silicon Solar Cells Enabling Efficiency over 21.6%”. en. In: *Advanced Functional Materials* 30.50 (2020), p. 2005554.

[46] Bert Conings et al. “Intrinsic Thermal Instability of Methylammonium Lead Trihalide Perovskite”. en. In: *Advanced Energy Materials* 5.15 (2015), p. 1500477.

[47] Eric T. Hoke et al. “Reversible photo-induced trap formation in mixed-halide hybrid perovskites for photovoltaics”. en. In: *Chemical Science* 6.1 (2015), pp. 613–617.

[48] Yutao Wang et al. “Phase segregation in inorganic mixed-halide perovskites: from phenomena to mechanisms”. EN. In: *Photonics Research* 8.11 (Nov. 2020), A56–A71.

[49] Jin Il Kwak et al. “Comparative toxicity of potential leachates from perovskite and silicon solar cells in aquatic ecosystems”. In: *Aquatic Toxicology* 237 (Aug. 2021), p. 105900.

[50] Gill Sang Han et al. “Cutting-Edge Studies Toward Commercialization of Large Area Solution-Processed Perovskite Solar Cells”. en. In: *Advanced Materials Technologies* 8.20 (2023), p. 2201387.

[51] Henry J. Snaith et al. “Anomalous Hysteresis in Perovskite Solar Cells”. In: *The Journal of Physical Chemistry Letters* 5.9 (May 2014), pp. 1511–1515.

[52] Pengyun Liu et al. “Fundamental Understanding of Photocurrent Hysteresis in Perovskite Solar Cells”. en. In: *Advanced Energy Materials* 9.13 (2019), p. 1803017.

[53] Yaoguang Rong et al. “Tunable hysteresis effect for perovskite solar cells”. en. In: *Energy & Environmental Science* 10.11 (Nov. 2017), pp. 2383–2391.

[54] Naveen Kumar Elumalai and Ashraf Uddin. “Hysteresis in organic-inorganic hybrid perovskite solar cells”. In: *Solar Energy Materials and Solar Cells* 157 (Dec. 2016), pp. 476–509.

[55] Michele De Bastiani et al. “Ion Migration and the Role of Preconditioning Cycles in the Stabilization of the J–V Characteristics of Inverted Hybrid Perovskite Solar Cells”. In: *Advanced Energy Materials* 6.2 (2016), p. 1501453.

[56] Daniel Walter et al. “Transient Photovoltage in Perovskite Solar Cells: Interaction of Trap-Mediated Recombination and Migration of Multiple Ionic Species”. In: *The Journal of Physical Chemistry C* 122.21 (May 2018), pp. 11270–11281.

[57] Jon M. Azpiroz et al. “Defect migration in methylammonium lead iodide and its role in perovskite solar cell operation”. en. In: *Energy & Environmental Science* 8.7 (2015), pp. 2118–2127.

[58] Christopher Eames et al. “Ionic transport in hybrid lead iodide perovskite solar cells”. en. In: *Nature Communications* 6.1 (June 2015), p. 7497.

[59] W. Tress et al. “Understanding the rate-dependent J – V hysteresis, slow time component, and aging in CH 3 NH 3 PbI 3 perovskite solar cells: the role of a compensated electric field”. en. In: *Energy & Environmental Science* 8.3 (2015), pp. 995–1004.

[60] Yuchuan Shao et al. “Origin and elimination of photocurrent hysteresis by fullerene passivation in CH3NH3PbI3 planar heterojunction solar cells”. en. In: *Nature Communications* 5.1 (Dec. 2014), p. 5784.

[61] Jixian Xu et al. “Perovskite–fullerene hybrid materials suppress hysteresis in planar diodes”. en. In: *Nature Communications* 6.1 (May 2015), p. 7081.

[62] Andreas Baumann et al. “Identification of Trap States in Perovskite Solar Cells”. In: *The Journal of Physical Chemistry Letters* 6.12 (June 2015), pp. 2350–2354.

[63] Rik van Heerden et al. “Slow Shallow Energy States as the Origin of Hysteresis in Perovskite Solar Cells”. In: *Frontiers in Photonics* 3 (2022).

[64] Stefan A. L. Weber et al. “How the formation of interfacial charge causes hysteresis in perovskite solar cells”. en. In: *Energy & Environmental Science* 11.9 (Sept. 2018), pp. 2404–2413.

[65] Rafael S. Sanchez et al. “Slow Dynamic Processes in Lead Halide Perovskite Solar Cells. Characteristic Times and Hysteresis”. In: *The Journal of Physical Chemistry Letters* 5.13 (July 2014), pp. 2357–2363.

[66] Emilio J. Juarez-Perez et al. “Photoinduced Giant Dielectric Constant in Lead Halide Perovskite Solar Cells”. In: *The Journal of Physical Chemistry Letters* 5.13 (July 2014), pp. 2390–2394.

[67] Osbel Almora et al. “Capacitive Dark Currents, Hysteresis, and Electrode Polarization in Lead Halide Perovskite Solar Cells”. In: *The Journal of Physical Chemistry Letters* 6.9 (May 2015), pp. 1645–1652.

[68] Jing Wei et al. “Hysteresis Analysis Based on the Ferroelectric Effect in Hybrid Perovskite Solar Cells”. In: *The Journal of Physical Chemistry Letters* 5.21 (Nov. 2014), pp. 3937–3945.

[69] Hsin-Wei Chen et al. “Emergence of Hysteresis and Transient Ferroelectric Response in Organo-Lead Halide Perovskite Solar Cells”. In: *The Journal of Physical Chemistry Letters* 6.1 (Jan. 2015), pp. 164–169.

[70] Jarvist M. Frost et al. “Atomistic Origins of High-Performance in Hybrid Halide Perovskite Solar Cells”. In: *Nano Letters* 14.5 (May 2014), pp. 2584–2590.

[71] Fan Wu, Rajesh Pathak, and Qiquan Qiao. “Origin and alleviation of J-V hysteresis in perovskite solar cells: A short review”. In: *Catalysis Today*. Preface to the Special Issue In Honor of Dr. E.Gerry Meyer 374 (Aug. 2021), pp. 86–101.

[72] Yunkang Cui et al. “Correlating Hysteresis and Stability with Organic Cation Composition in the Two-Step Solution-Processed Perovskite Solar Cells”. In: *ACS Applied Materials & Interfaces* 12.9 (Mar. 2020), pp. 10588–10596.

[73] Aaesha Alnuaimi, Ibraheem Almansouri, and Ammar Nayfeh. “Effect of mobility and band structure of hole transport layer in planar heterojunction perovskite solar cells using 2D TCAD simulation”. en. In: *Journal of Computational Electronics* 15.3 (Sept. 2016), pp. 1110–1118.

[74] Mohamed Okil et al. “Investigation of Polymer/Si Thin Film Tandem Solar Cell Using TCAD Numerical Simulation”. en. In: *Polymers* 15.9 (Jan. 2023), p. 2049.

[75] Manvika Singh et al. “On current collection from supporting layers in perovskite/c-Si tandem solar cells: 48th IEEE Photovoltaic Specialists Conference, PVSC 2021”. In: *2021 IEEE 48th Photovoltaic Specialists Conference, PVSC 2021*. Conference Record of the IEEE Photovoltaic Specialists Conference (2021), pp. 303–305.

[76] Kumudini Ganesh and Revathy Padmanabhan. “Modeling of Hysteresis in Perovskite-Silicon Tandem Solar Cells”. In: *2021 IEEE 16th Nanotechnology Materials and Devices Conference (NMDC)*. Dec. 2021, pp. 1–5.

[77] Rudi Santbergen et al. “GenPro4 Optical Model for Solar Cell Simulation and Its Application to Multijunction Solar Cells”. In: *IEEE Journal of Photovoltaics* 7.3 (May 2017), pp. 919–926.

[78] Donald A. Neamen. *Semiconductor physics and devices: basic principles*. en. 4. ed. New York, NY: McGraw-Hill, 2012.

[79] S.M Sze and Kwok K. Ng. *Physics of Semiconductor Devices*.

[80] Synopsys. *Sentaurus Device User Guide - 2015.6*.

[81] *Degeneracy Factor - an overview | ScienceDirect Topics*.

[82] Hsin-Sheng Duan et al. “The identification and characterization of defect states in hybrid organic–inorganic perovskite photovoltaics”. en. In: *Physical Chemistry Chemical Physics* 17.1 (Dec. 2014), pp. 112–116.

[83] Sung Heo et al. “Deep level trapped defect analysis in CH3NH3PbI3 perovskite solar cells by Deep Level Transient Spectroscopy”. In: *Energy Environ. Sci.* 10 (Feb. 2017), p. 1128.

[84] James M. Ball and Annamaria Petrozza. “Defects in perovskite-halides and their effects in solar cells”. en. In: *Nature Energy* 1.11 (Oct. 2016), p. 16149.

[85] Wan-Jian Yin, Tingting Shi, and Yanfa Yan. “Unusual Defect Physics in CH3NH3PbI3 Perovskite Solar Cell Absorber”. In: *Applied Physics Letters* 104 (Feb. 2014), pp. 063903–063903.

[86] Michael Agiorgousis et al. “Strong Covalency-Induced Recombination Centers in Perovskite Solar Cell Material CH(3)NH(3)Pbl(3)”. In: *Journal of the American Chemical Society* 136 (Sept. 2014).

[87] Zhenyi Ni et al. “Resolving spatial and energetic distributions of trap states in metal halide perovskite solar cells”. In: *Science* 367.6484 (Mar. 2020), pp. 1352–1358.

[88] John F. Wager. “Real- and reciprocal-space attributes of band tail states”. In: *AIP Advances* 7.12 (Dec. 2017), p. 125321.

[89] Dale J. Igram. “A Topological Explanation of the Urbach Tail”. en. PhD thesis. Ohio University, 2016.

[90] Y. Pan et al. “Atomistic Origin of Urbach Tails in Amorphous Silicon”. In: *Physical Review Letters* 100.20 (May 2008), p. 206403.

[91] Stefaan De Wolf et al. “Organometallic Halide Perovskites: Sharp Optical Absorption Edge and Its Relation to Photovoltaic Performance”. In: *The Journal of Physical Chemistry Letters* 5.6 (Mar. 2014), pp. 1035–1039.

[92] Martin Ledinsky et al. “Temperature Dependence of the Urbach Energy in Lead Iodide Perovskites”. In: *The Journal of Physical Chemistry Letters* 10.6 (Mar. 2019), pp. 1368–1373.

[93] Christoph Messmer et al. “Toward more reliable measurement procedures of perovskite-silicon tandem solar cells: The role of transient device effects and measurement conditions”. en. In: *Progress in Photovoltaics: Research and Applications* n/a.n/a ().

[94] Amalie Dualeh et al. “Impedance Spectroscopic Analysis of Lead Iodide Perovskite-Sensitized Solid-State Solar Cells”. In: *ACS Nano* 8.1 (Jan. 2014), pp. 362–373.

[95] Philip Calado et al. “Evidence for ion migration in hybrid perovskite solar cells with minimal hysteresis”. en. In: *Nature Communications* 7.1 (Dec. 2016), p. 13831.

[96] Mariona Coll et al. “Polarization Switching and Light-Enhanced Piezoelectricity in Lead Halide Perovskites”. In: *The Journal of Physical Chemistry Letters* 6.8 (Apr. 2015), pp. 1408–1413.

[97] Giles E. Eperon et al. “Inorganic caesium lead iodide perovskite solar cells”. en. In: *Journal of Materials Chemistry A* 3.39 (2015), pp. 19688–19695.

[98] George Alexandru Nemnes et al. “How measurement protocols influence the dynamic J-V characteristics of perovskite solar cells: Theory and experiment”. In: *Solar Energy* 173 (Oct. 2018), pp. 976–983.

[99] Jiayi Wang. “High Performance Wide Bandgap Perovskite Solar Cell Based on Interface Engineering”. en. In: (May 2023).

[100] M. Vogel et al. “On the function of a bathocuproine buffer layer in organic photovoltaic cells”. In: *Applied Physics Letters* 89.16 (Oct. 2006), p. 163501.

[101] Pengjun Zhao, Byeong Jo Kim, and Hyun Jung. “Passivation in perovskite solar cells: A review”. In: *Materials Today Energy* 7 (Feb. 2018), pp. 267–286.

[102] Hang Cheong Sio et al. “Improving doped polycrystalline silicon passivating contacts with magnesium fluoride”. In: *Solar Energy Materials and Solar Cells* 254 (June 2023), p. 112251.

[103] Arvind Shah. *Hydrogenated Amorphous Silicon - an overview | ScienceDirect Topics*.

[104] Paul Procel et al. “The role of heterointerfaces and subgap energy states on transport mechanisms in silicon heterojunction solar cells”. en. In: *Progress in Photovoltaics: Research and Applications* 28.9 (2020), pp. 935–945.

[105] Jin Hyuck Heo et al. “Planar CH3NH3PbI3 Perovskite Solar Cells with Constant 17.2% Average Power Conversion Efficiency Irrespective of the Scan Rate”. In: *Advanced Materials* 27.22 (2015), pp. 3424–3430.

[106] Matic Herman, Marko Jankovec, and Marko Topič. “Optimal I-V Curve Scan Time of Solar Cells and Modules in Light of Irradiance Level”. en. In: *International Journal of Photoenergy* 2012.1 (2012), p. 151452.

[107] Wolfgang Tress et al. “Inverted Current–Voltage Hysteresis in Mixed Perovskite Solar Cells: Polarization, Energy Barriers, and Defect Recombination”. en. In: *Advanced Energy Materials* 6.19 (2016), p. 1600396.

[108] Dong-Ho Kang and Nam-Gyu Park. “On the Current–Voltage Hysteresis in Perovskite Solar Cells: Dependence on Perovskite Composition and Methods to Remove Hysteresis”. en. In: *Advanced Materials* 31.34 (2019), p. 1805214.

[109] Dongguen Shin et al. “Mechanism and Timescales of Reversible p-Doping of Methylammonium Lead Triiodide by Oxygen”. en. In: *Advanced Materials* 33.23 (2021), p. 2100211.

[110] Martin Thomas Neukom et al. “Why perovskite solar cells with high efficiency show small IV-curve hysteresis”. In: *Solar Energy Materials and Solar Cells* 169 (Sept. 2017), pp. 159–166.

[111] Bo Chen et al. “Origin of J–V Hysteresis in Perovskite Solar Cells”. In: *The Journal of Physical Chemistry Letters* 7.5 (Mar. 2016), pp. 905–917.

[112] Stephan van Reenen, Martijn Kemerink, and Henry J. Snaith. “Modeling Anomalous Hysteresis in Perovskite Solar Cells”. In: *The Journal of Physical Chemistry Letters* 6.19 (Oct. 2015), pp. 3808–3814.

[113] Heejae Lee et al. “Direct Experimental Evidence of Halide Ionic Migration under Bias in CH3NH3PbI3–xClx-Based Perovskite Solar Cells Using GD-OES Analysis”. In: *ACS Energy Letters* 2.4 (Apr. 2017), pp. 943–949.

[114] Shynggys Zhumagali et al. “Linked Nickel Oxide/Perovskite Interface Passivation for High-Performance Textured Monolithic Tandem Solar Cells”. en. In: *Advanced Energy Materials* 11.40 (2021), p. 2101662.

[115] M. H. Du. “Efficient carrier transport in halide perovskites: theoretical perspectives”. en. In: *Journal of Materials Chemistry A* 2.24 (May 2014), pp. 9091–9098.

A

Additional Theory

A.1. Drift and diffusion

The charge carriers mentioned before do not stay in one place, they move. The movement of these carriers is called transport. Carrier transport is mainly governed by two basic transport mechanisms: drift and diffusion.

When an electric field is applied to a semiconductor, a force will be produced on electrons and holes which causes them to move. This movement of the charge carriers due to the electric field is called drift. Diffusion, on the other hand, is caused by density gradients. Whenever there are more carriers in one area than another, the carriers move from the higher concentration area towards the low concentration region. This is called diffusion. The drift-diffusion model uses the basic semiconductor equations. These equations can be divided into three classes: current-density equations, continuity equations and Poisson's equation.

The current density equation is made up of sum of the drift and diffusion currents. The generalized equation for three dimensions is:

$$\vec{J} = en\mu_n E_x + ep\mu_p E_x + eD_n \nabla n - eD_p \nabla p = \vec{J_n} + \vec{J_p} \tag{A.1}$$

With μ being the charge carrier mobility, n and p the electron and hole concentration respectively, D the diffusion coefficient and e the elementary charge. The equation can be split into the electron and hole currents.

$$\vec{J_n} = en\mu_n E_x + eD_n \nabla n \tag{A.2}$$

$$\vec{J_p} = ep\mu_p E_x - eD_p \nabla p \tag{A.3}$$

The continuity equations are used to explain the change of charge carrier concentration based on particle fluxes, recombination and generation of carriers within the device. The equations are:

$$\frac{\partial n}{\partial t} = \frac{1}{e} \nabla \cdot \vec{J_n} + G - R \tag{A.4}$$

$$\frac{\partial p}{\partial t} = -\frac{1}{e} \nabla \cdot \vec{J_p} + G - R \tag{A.5}$$

With G being the generation rate and R the recombination rate.
The last equation is Poisson's equation. Poisson's equation knows many forms but generally it describes a potential field caused by an electric density. The form of Poisson's equation used by Sentaurus is:

$$\nabla \cdot (\epsilon \nabla \phi) = -q(p - n + N_D - N_A) - \rho_{trap} \tag{A.6}$$

In this equation, ϵ is the electrical permittivity, q the elementary electronic charge, N_D the concentration of doped donors, N_A the concentration of doped acceptors and lastly, ρ_{trap} the charge density contributed by traps and fixed charges.